CME Article

Optimized Three-Dimensional Fast-Spin-Echo MRI

CME

John P. Mugler III, PhD*

This article is accredited as a journal-based CME activity. If you wish to receive credit for this activity, please refer to the website: www.wileyhealthlearning.com/jmri

ACCREDITATION AND DESIGNATION STATEMENT

Blackwell Futura Media Services designates this journal based CME activity for a maximum of 1 *AMA PRA Category 1 Credit™*. Physicians should only claim credit commensurate with the extent of their participation in the activity.

Blackwell Futura Media Services is accredited by the Accreditation Council for Continuing Medical Education to provide continuing medical education for physicians.

EDUCATIONAL OBJECTIVES

Upon completion of this educational activity, participants will be better able to:

1. Describe pulse-sequence design strategies used to optimize single-slab 3D fast-spin-echo imaging.
2. Identify important differences between optimized single-slab 3D fast-spin-echo imaging and conventional 2D fast-spin-echo imaging, particularly concerning image contrast behavior and artifacts.

ACTIVITY DISCLOSURES

No commercial support has been accepted related to the development or publication of this activity.

Faculty Disclosures:
Editor-in-Chief: Mark E. Schweitzer, MD, discloses DSMB work for Paradigm Spine, and consultation for MMI.

CME Editor: Scott B. Reeder, MD, PhD has no conflicts of interest to disclose.

CME Committee: Pratik Mukherjee, MD, PhD, Shreyas Vasanawala, MD, PhD, Bonnie Joe, MD, PhD, Tim Leiner, MD, PhD, Sabine Weckbach, MD, and Frank Korosec, PhD have no conflicts of interest to disclose. Scott K. Nagle, MD, PhD discloses a personal shareholder investment in GE. Mustafa R. Bashir, MD discloses research support from Bracco Diagnostics and Siemens Healthcare, and consultant honorarium from Bayer Pharmaceuticals.

Author: John P. Mugler III, PhD discloses research support and consulting fees from Siemens Healthcare.

This manuscript underwent peer review in line with the standards of editorial integrity and publication ethics maintained by Journal of Magnetic Resonance Imaging. The peer reviewers have no relevant financial relationships. The peer review process for Journal of Magnetic Resonance Imaging is double-blinded. As such, the identities of the reviewers are not disclosed in line with the standard accepted practices of medical journal peer review.

Conflicts of interest have been identified and resolved in accordance with Blackwell Futura Media Services' Policy on Activity Disclosure and Conflict of Interest.

INSTRUCTIONS ON RECEIVING CREDIT

For information on applicability and acceptance of CME credit for this activity, please consult your professional licensing board.

This activity is designed to be completed within an hour; physicians should claim only those credits that reflect the time actually spent in the activity. To successfully earn credit, participants must complete the activity during the valid credit period.

Follow these steps to earn credit:

- Log on to www.wileyhealthlearning.com
- Read the target audience, educational objectives, and activity disclosures.
- Read the article in print or online format.
- Reflect on the article.
- Access the CME Exam, and choose the best answer to each question.
- Complete the required evaluation component of the activity.

This activity will be available for CME credit for twelve months following its publication date. At that time, it will be reviewed and potentially updated and extended for an additional period.

Department of Radiology and Medical Imaging, University of Virginia School of Medicine, Charlottesville, Virginia, USA.
*Address reprint requests to: J.P.M., University of Virginia, P.O. Box 801339, Charlottesville, VA 22908. E-mail: john.mugler@virginia.edu
Received August 12, 2013; Accepted October 31, 2013.
DOI 10.1002/jmri.24542
View this article online at wileyonlinelibrary.com.

Spin-echo-based acquisitions are the workhorse of clinical MRI because they provide a variety of useful image contrasts and are resistant to image artifacts from radio-frequency or static field inhomogeneity. Three-dimensional (3D) acquisitions provide datasets that can be retrospectively reformatted for viewing in freely selectable orientations, and are thus advantageous for evaluating the complex anatomy associated with many clinical applications of MRI. Historically, however, 3D spin-echo-based acquisitions have not played a significant role in clinical MRI due to unacceptably long acquisition times or image artifacts associated with details of the acquisition method. Recently, optimized forms of 3D fast/turbo spin-echo imaging have become available from several MR-equipment manufacturers (for example, CUBE [GE], SPACE [Siemens], and VISTA [Philips]). Through specific design strategies and optimization, including short non–spatially selective radio-frequency pulses to significantly shorten the echo spacing and variable flip angles for the refocusing radio-frequency pulses to suppress blurring or considerably lengthen the useable duration of the spin-echo train, these techniques permit single-slab 3D imaging of sizeable volumes in clinically acceptable acquisition times. These optimized fast/turbo spin-echo pulse sequences provide a robust and flexible approach for 3D spin-echo-based imaging with a broad range of clinical applications.

Key Words: RARE; fast spin echo; turbo spin echo; 3D FSE; 3D TSE; variable flip angles
J. Magn. Reson. Imaging 2014;39:745–767.

SPIN-ECHO-BASED acquisitions are used widely in clinical MRI because they provide a variety of image contrasts that highlight pathology and are resistant to image artifacts from radio-frequency (RF) and static field inhomogeneity. In particular, "fast-spin-echo" (FSE) or "turbo-spin-echo" (TSE) pulse sequences, which are optimized derivatives of the RARE technique (1), find use for a broad spectrum of MRI applications because these methods combine the desirable properties of spin-echo-based acquisitions with the speed advantage of collecting multiple lines of phase-encoding (*k*-space) data following each excitation RF pulse. This speed advantage is the rationale for using the term "fast" or "turbo" in the name for these techniques. Without preference for a particular manufacturer's implementation, "fast spin echo," or "FSE" is used herein to refer to this type of pulse sequence.

Three-dimensional (3D) acquisitions are advantageous for evaluating complex anatomy because the corresponding datasets can be retrospectively reformatted for viewing in freely selectable orientations. Thus a single 3D acquisition can replace several comparable multi-slice two-dimensional (2D) acquisitions. Three-dimensional datasets are also desirable for quantitative postprocessing analyses, such as applied to Alzheimer's disease in the ADNI project (2). For FSE, multi-slab 3D implementations (3,4) have been available for roughly 20 years, although the multi-slab approach is prone to artifacts at the boundaries between adjacent slabs, degrading the quality of multi-planar reformatted images (5). Even though technical approaches for mitigating slab-boundary artifacts have been developed (5,6), multi-slab 3D-FSE imaging has not gained widespread clinical use. As a result, clinical FSE imaging is typically performed using multi-slice 2D techniques, and datasets with identical timing parameters, but different orientations, are often acquired for a given patient.

Within just the past few years, several MR-equipment manufacturers have offered optimized versions of 3D FSE that are suitable for "single-slab" imaging of sizeable volumes (e.g., the whole head or knee) in clinically acceptable acquisition times. By collecting all data from a single, thick slab, the slab-boundary artifacts present in multi-slab imaging are eliminated, and high-quality images reformatted in multiple orientations can be obtained. Examples of such single-slab 3D-FSE methods include CUBE (GE Healthcare), SPACE (Sampling Perfection with Application optimized Contrasts by using different flip angle Evolutions; Siemens Healthcare) and VISTA (Volumetric ISotropic TSE Acquisition; Philips Healthcare).

Early applications of optimized single-slab 3D FSE focused on the brain (7–10). As these pulse sequences became more widely available, applications expanded beyond the brain (11–28) and spine (29,30), into the body (31–42) and musculoskeletal system. The high-resolution 3D datasets available from optimized 3D FSE are particularly appealing for assessing the complex anatomy of the joints (43), which has led to studies involving the knee (44–55), ankle (56–58), shoulder (59–61), and wrist (62,63). The flow characteristics associated with optimized 3D FSE also provide the opportunity for interesting applications in the vasculature; including approaches for assessing the lumen (MR angiography) (64–72) and vessel wall (72–76).

The purpose of this article is to describe the design and characteristics of optimized single-slab 3D-FSE pulse sequences. As background for this discussion, we begin by reviewing major features of a 2D-FSE pulse sequence, differences between single-slab and multi-slab 3D imaging, as well as basic functional properties of RF pulses. The last topic is important for understanding the behavior of refocusing RF pulses with variable flip angles, as often used in single-slab 3D-FSE imaging. Readers well-versed in these introductory topics may skip the Background section without loss of continuity.

BACKGROUND

2D Fast-Spin-Echo Imaging

As noted above, today's 2D-FSE pulse sequences are optimized versions (77,78) of the RARE (Rapid Acquisition with Relaxation Enhancement) technique introduced by Hennig et al in 1986 (1). Key features of a 2D-FSE pulse sequence are illustrated by the timing diagram in Figure 1. For the typical implementation, a 90° (excitation) RF pulse is followed by a "train" of equally spaced 180° (refocusing) RF pulses, generating a train of spin echoes, as shown on the line labeled

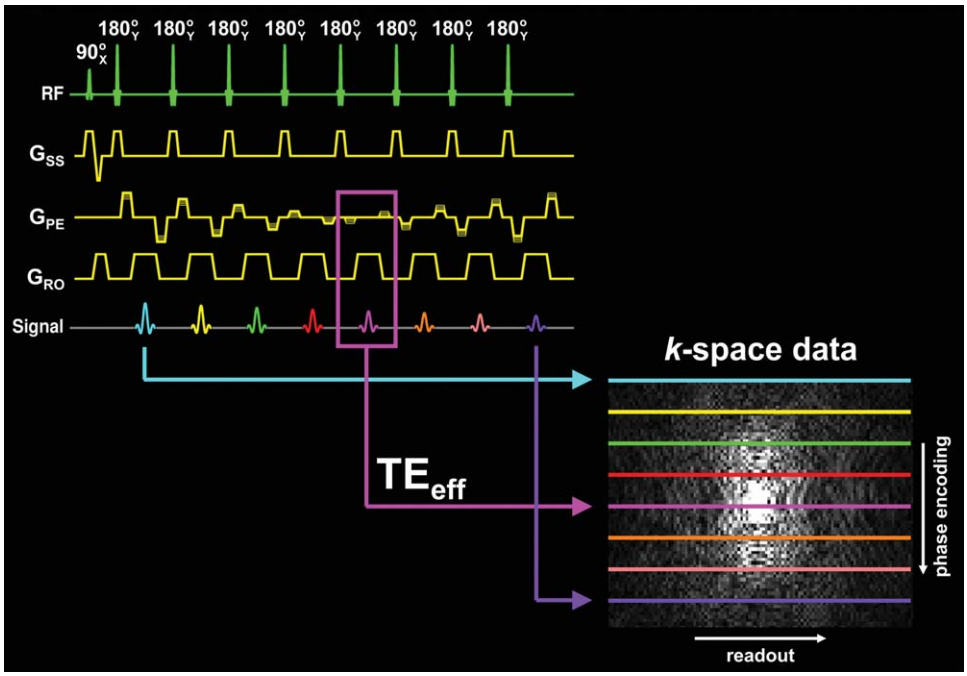

Figure 1. Two-dimensional fast-spin-echo imaging. The timing diagram for one repetition of a typical 2D-FSE pulse sequence is shown on the upper left. In this example, eight spin echoes (echo train length = 8) are collected following the 90° excitation RF pulse. The manner in which data corresponding to these eight spin echoes are placed into *k*-space along the phase-encoding direction is illustrated on the lower right. The fifth echo corresponds to the effective echo time (TE_{eff}) for the pulse sequence. For simplicity, additional gradient waveforms typically applied along the slice-select and readout axes, used for "spoiling" ("crushing") undesired signals, are omitted. (RF, radio frequency; G_{SS}, slice-select gradient; G_{PE}, in-plane phase-encoding gradient; G_{RO}, readout [frequency-encoding] gradient.)

"Signal" in Figure 1. Each of these spin echoes is used to acquire a different line of *k*-space data along the phase-encoding direction (lower right of Fig. 1). As the pulse sequence is repeated, the phase-encoding gradient amplitudes are incremented so that the remaining lines of *k*-space are filled in an interleaved manner.

Because a range of echo times are represented in the *k*-space data, a single echo time (TE) does not fully describe the data. For this reason, instead of using the term TE to denote the associated contrast behavior as in conventional spin-echo imaging, FSE acquisitions are said to have an effective echo time (TE_{eff}), which is the echo time corresponding to data in the central region of *k*-space. For the example shown in Figure 1, TE_{eff} is the value corresponding to the 5th echo. Recall that the data in the central region of *k*-space determine the gross structure and contrast of the image. Thus, for example, if the spacing between successive echoes (Echo SPacing, ESP) in Figure 1 is 20 ms, data in the central region of *k*-space correspond to an echo time of 100 ms (5 × ESP), and the FSE image demonstrates image contrast substantially the same as that for a conventional spin-echo image having an echo time of 100 ms. However, even when TE for a conventional spin-echo acquisition equals TE_{eff} for an FSE acquisition, there are subtle differences between the corresponding images, which have been discussed thoroughly in the literature (79–83). Herein, the term TE_{eff} will be used to refer to the echo time at which data corresponding to the center of *k*-space are acquired, although we will see that the echo time reflecting image contrast for single-slab 3D FSE may be very different from that corresponding to the center of *k*-space.

The number of 180° (refocusing) RF pulses, which equals the number of spin echoes generated, is termed the Echo-Train Length (ETL). The ETL values used for clinical FSE imaging typically fall into one of two ranges. For routine imaging with fairly high spatial resolution, ETL typically ranges from a few echoes (for short TE_{eff} values) up to roughly 30 echoes (for moderate to long TE_{eff} values). For this range, the total number of phase-encoding steps is usually many times larger than the ETL, and the data acquired as the pulse sequence repeats are interleaved in *k*-space using one of several well-established schemes. For single-shot FSE imaging, the ETL ranges from tens of echoes up to more than 100 echoes, and is chosen to provide all of the data required to generate an image from the echoes acquired following a single excitation RF pulse. In this case, a scheme for interleaving data in *k*-space from multiple excitations is, of course, not required.

Single-Slab Versus Multi-slab 3D Imaging

MR images covering an anatomical region of interest are typically obtained using either a set of 2D slices (Fig. 2, left) or a 3D volume (Fig. 2, center). Recall, compared with 2D slice-selective imaging, that a 3D acquisition uses an additional phase-encoding gradient to perform spatial encoding along the slice-select direction, generating a set of contiguous slices within the volume. For conventional spin-echo or gradient-

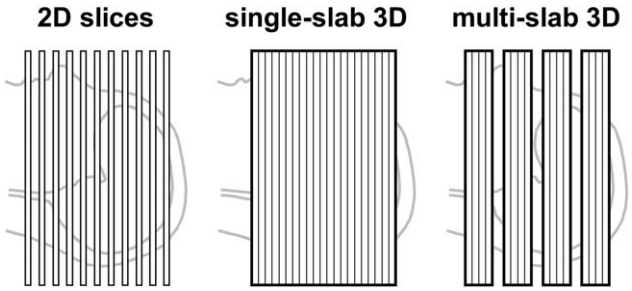

Figure 2. Basic strategies for obtaining a set of MR images: 2D slices, single-slab 3D, and multi-slab 3D. In 2D imaging, the slices are excited individually, whereas, in 3D imaging, phase encoding is used along the slice-select direction to obtain a set of contiguous slices within the single, excited volume. Multi-slab 3D imaging is a hybrid of the 2D and (single-slab) 3D approaches.

echo pulse sequences, the acquisition time for 3D imaging equals the repetition time (TR) multiplied by the product of the number of phase-encoding steps for the second dimension and that for the third dimension. Therefore, if a large number of slices is desired in the third dimension, the imaging time is quite long unless TR is relatively short. For FSE, the acquisition time for 3D imaging is reduced in proportion to the ETL. Nonetheless, for imaging a sizeable volume such as the whole head with high spatial resolution, the acquisition time for a 3D implementation of FSE using ETLs in the range typical for clinical MRI (<30) remains too long for routine application.

Multi-slab 3D imaging is a hybrid of 2D and 3D imaging wherein a set of thick slices, or "slabs," is excited, and each slab is in turn phase-encoded along the third dimension to yield a set of contiguous slices (Fig. 2, right). Because collection of *k*-space data for the slabs in a multi-slab 3D acquisition is interleaved during the repetition time, analogous to slices in a multi-slice 2D acquisition, the imaging time for multi-slab 3D FSE is clinically practical, although, as noted above, this approach has failed to gain widespread clinical use. In the context of multi-slab 3D imaging, a "true" (single-volume) 3D acquisition is referred to as single-slab 3D imaging.

Roles of RF Pulses

Although RF pulses are typically described in terms of the specific associated flip angles (e.g., 90° or 180° as shown in Fig. 1), it is nonetheless useful to consider the "role" that the RF pulse is intended to play in the pulse sequence, in addition to its flip angle. In this section, three common roles of RF pulses are reviewed: excitation, refocusing, and store/recall. Figure 3 illustrates the effects of RF pulses on the magnetization using diagrams of the magnetization vectors associated with a voxel of tissue. (For simplicity, the RF pulses themselves are omitted from the vector diagrams.) In these diagrams, a yellow vector (e.g., Fig. 3a) represents the total magnetization for the voxel, red and green vectors (e.g., Fig. 3c) represent magnetization associated with regions within the voxel which experience different resonance frequencies due to static field inhomogeneity and/or applied magnetic field gradients, and two-color vectors (e.g., Fig. 3h) represent overlapping red and green vectors of the same length. Because each red or green vector corresponds to a small fraction of the voxel volume, the length of each vector is actually proportionately smaller than that of the yellow vector, which represents the whole voxel. (The sum of all red and green vectors equals the total magnetization associated with the voxel.) However, for clarity in the vector diagrams, the initial lengths of yellow, red and green vectors are shown to be the same.

The diagrams in Figure 3a–e illustrate the excitation and refocusing roles of RF pulses in the familiar context of generating a spin echo. In general, the purpose of an excitation RF pulse is to transfer some or all of the longitudinal (z) magnetization to the transverse (x–y) plane for the purpose of subsequently producing an MR signal. In Figure 3a,b, the result of applying a 90° excitation RF pulse about the x-axis is shown, wherein the magnetization vector is rotated through an angle of 90°, from the z-axis to the y-axis. Following excitation, static-field inhomogeneity and any applied magnetic field gradients cause transverse magnetization vectors associated with different regions within the voxel to have different resonance frequencies and therefore to precess at different rates. As a result the transverse magnetization "dephases" as shown in Figure 3c wherein, during a time period equal to TE/2, the green vectors have rotated clockwise about the z-axis due to precessing faster than the average resonance frequency for the voxel, and the red vectors have rotated counterclockwise due to precessing slower than the average resonance frequency. Next, a refocusing RF pulse is applied. In general, the purpose of a refocusing RF pulse is to change the orientations of the magnetization vectors relative to one another so that, following the same amount of precession for each vector as occurred preceding the RF pulse, the magnetization vectors fully or partially align with one another to yield an echo. The exemplary refocusing RF pulse has a flip angle of 180°, and, as seen by comparing Figure 3c to Figure 3d, a 180° refocusing RF pulse applied about the y-axis flips the magnetization vectors from one side of the transverse plane to the other, thus exchanging the red (slow) and green (fast) vectors. Following the refocusing RF pulse, the green vectors continue to rotate clockwise about the z-axis at the same rates, and likewise the red vectors continue to rotate counterclockwise, again during a time period equal to TE/2. As a result, the magnetization "rephases" and a spin echo is formed as the vectors come back into alignment at the echo time (Fig. 3e). (This, of course, assumes that the effects of any magnetic field gradients applied before and after the refocusing RF pulse are equivalent.) Neglecting T2 relaxation and diffusion effects, the spin echo has the same magnitude as the magnetization that existed immediately after excitation (Fig. 3b).

For most techniques used in clinical MRI, the primary role of an RF pulse is either excitation or refocusing. However, optimized single-slab 3D-FSE

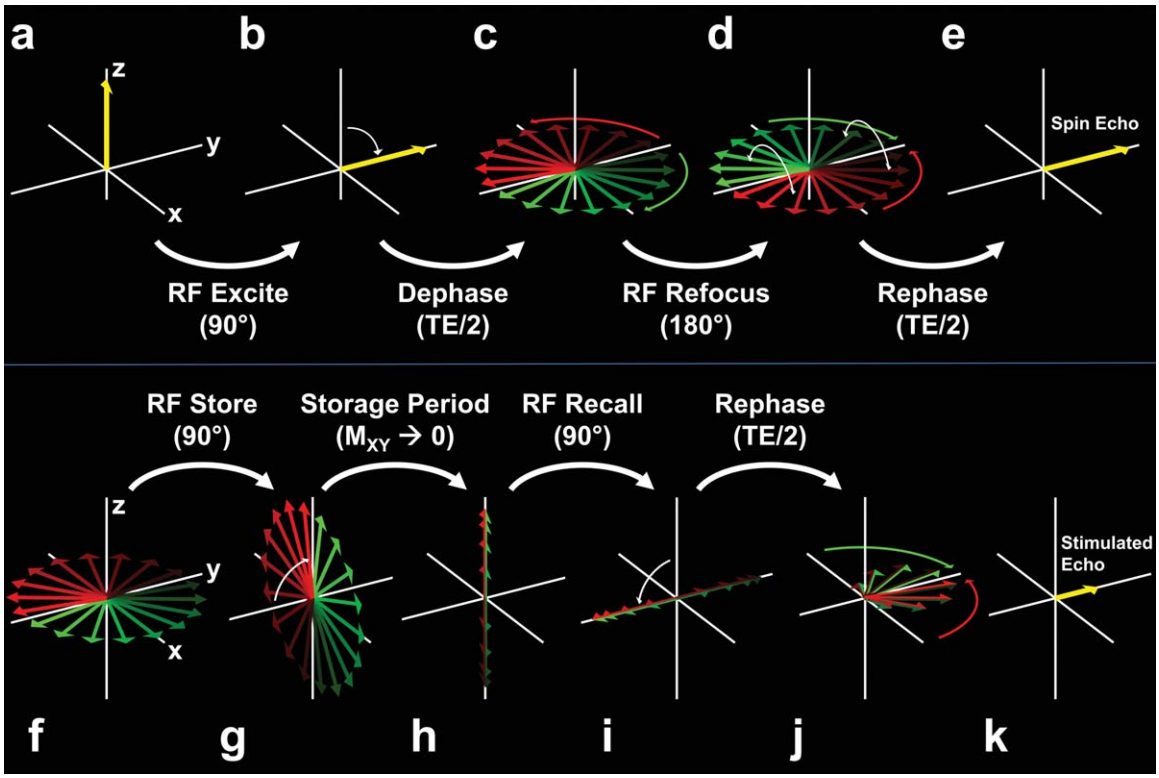

Figure 3. Excitation, refocusing, and store/recall roles of RF pulses. **a–e:** Excitation and refocusing are illustrated in the context of generating a spin echo. A 90° excitation RF pulse rotates the longitudinal magnetization for the voxel (yellow vector in [a]) to the transverse plane (b). Transverse magnetization vectors corresponding to different regions within the voxel (red and green vectors) precess at different rates, due to static-field inhomogeneity and/or magnetic field gradients, and thereby dephase in the transverse plane (c). A 180° refocusing RF pulse rotates the vectors about the y-axis, exchanging the red and green vectors (d). With continued precession, the vectors rephase, returning to alignment along the y-axis to form a spin echo (e). **f–k:** Store and recall functions of an RF pulse are illustrated in the context of generating a stimulated echo. Starting with magnetization that has dephased in the transverse plane following an excitation RF pulse ([f], same configuration as [c]), a 90° RF pulse stores the orientations of the transverse components of the magnetization vectors in the form of longitudinal (z-axis) magnetization (g). Following dephasing or decay of the remaining transverse components of the magnetization, red and green vectors overlap along the z-axis at the end of the storage period (h). Another 90° RF pulse recalls the longitudinal magnetization to the transverse plane (i), and through continued precession the vectors partially align with respect to the y-axis (j). The sum of the vectors within the voxel yields the stimulated echo (k). Effects of relaxation and diffusion are neglected in the diagrams, except during the storage period [from (g) to (h)] wherein, to simplify illustration of stimulated-echo formation, the transverse components of the magnetization shown in (g) are assumed to decay to zero by the end of the storage period. The coordinate (x, y, z) axes shown are in the "rotating" frame of reference.

imaging often uses refocusing RF pulses with variable flip angles, and for these pulses another echo-formation mechanism—the "stimulated" echo (84)—makes a major contribution to signal amplitudes during the echo train. Three RF pulses are required to generate a stimulated echo, as compared to two RF pulses to generate a spin echo.

The diagrams in Figure 3f–k illustrate generation of a stimulated echo resulting from the application of two 90° RF pulses following the excitation 90° RF pulse. To begin, Figure 3f shows transverse magnetization that has dephased during a time period of TE/2 following excitation (the vector configurations in Fig. 3f and 3c are identical). Next, the second 90° RF pulse is applied (about the x-axis) to "store" the orientations (phases) of the transverse components of the magnetization vectors in the form of longitudinal magnetization (Fig. 3g); note that, in Figure 3g, the component of each vector along the z-axis reflects its orientation (phase) in the transverse plane just before the RF pulse. For sufficient dephasing (from field inhomogeneity or applied gradients) during the "storage period" between the second and third 90° RF pulses, as typically occurs, the amplitude of the stimulated echo which forms following the third 90° RF pulse is determined only by the components of the magnetization vectors that were along the z-axis immediately following the second 90° RF pulse. That is, the transverse components of the magnetization vectors in Figure 3g do not make a net contribution to the stimulated echo. Therefore, to simplify illustration of stimulated-echo formation, we assume that the transverse components of the magnetization vectors decay to zero during the storage period between Figures 3g and 3h, so that in Figure 3h, at the end of the storage period, only longitudinal components of the magnetization remain, and red and green vectors now overlap along the z-axis. The third 90° RF pulse is applied (about the −x-axis) to "recall" the longitudinal magnetization to the transverse plane (Fig. 3i). During the rephasing

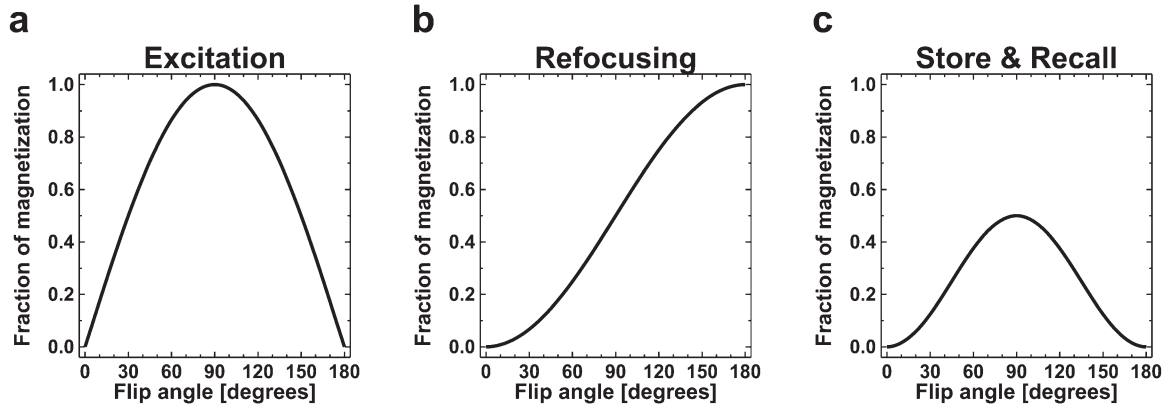

Figure 4. Efficiency of excitation, refocusing, and store/recall RF pulses versus flip angle. The plots show the fraction of magnetization that is excited (**a**), refocused (**b**), or stored and recalled (**c**) for flip angles between zero and 180°. Relaxation is neglected. The corresponding functional relationships are $\sin\theta$, $\sin^2(\theta/2)$ and $(\sin^2\theta)/2$ for excitation, refocusing, and store/recall, respectively.

period following the third 90° RF pulse, the green vectors again precess clockwise about the z-axis and the red vectors precess counterclockwise, analogous to the rephasing period for the spin echo. However, in contrast to the case for a spin echo, and as shown in Figure 3j, the red and green vectors do not all return to the positive y-axis at the end of the rephasing period. This is because their orientations in the transverse plane at the beginning of the period differed from those just before the store RF pulse was applied (compare Fig. 3i to Fig. 3f); thus some vectors overshoot the y-axis while others do not quite return to the y-axis. (For readers familiar with the "figure 8" configuration of the magnetization at the stimulated echo, the pattern in Figure 3j is simply the figure 8 pattern collapsed onto the transverse plane, which occurs in Figure 3j because it is assumed that the transverse components in Figure 3g decay to zero during the storage period.) Even so, the sum of the red and green vectors (after considering the relationship between the relative lengths of total [yellow] versus component [red and green] vectors) corresponds to the total magnetization vector for the voxel shown in Figure 3k. Neglecting relaxation and diffusion effects, the magnitude of this stimulated echo is half of that for the magnetization that existed immediately after excitation (Fig. 3b).

A key feature of stimulated-echo formation is that, between the store and recall RF pulses, the stored longitudinal magnetization decays according to the T1 relaxation time of the tissue. Thus, T1 plays a major role in determining the amplitude of a stimulated echo, while the amplitude of a spin echo is determined solely by T2. (The stimulated echo is also affected by T2 relaxation; T2 decay occurs during the time period between the first [excitation] and second [store] RF pulses, and during that between the third [recall] RF pulse and the echo time.) Because T1 is several times longer than T2 for many biological tissues, the time period between the excitation RF pulse and formation of an echo with a given signal amplitude can be made much longer for a stimulated echo than for a spin echo. As discussed in more detail later in the article, this basic property of stimulated echoes underlies the opportunity to use refocusing RF pulses with variable flip angles to greatly extend the useable duration of a spin-echo train for FSE imaging.

Other more complicated mechanisms of echo formation exist (85,86). For the interested reader, the extended-phase-graph approach described by Hennig (86) is a very useful tool for calculating and visualizing the myriad of signal pathways that can lead to echoes from a train of RF pulses. Nonetheless, a basic understanding of spin echoes and stimulated echoes is sufficient to qualitatively understand the motivation for and general properties of variable-flip-angle refocusing RF pulses for 3D FSE.

The plots in Figure 4 show the efficiency of an RF pulse for performing the individual roles (e.g., as illustrated in Fig. 3) of excitation (Fig. 4a), refocusing (Fig. 4b; generating a spin echo) or store/recall (Fig. 4c; generating a stimulated echo) as a function of flip angle. We see that a flip angle of 90° yields maximum excitation, as well as the maximum value for store/recall and a moderate value for refocusing. Furthermore, for any flip-angle value other than those close to zero or 180°, an RF pulse can have sizeable contributions as an excitation pulse, a refocusing pulse, and a store (or recall) pulse. Thus, over a wide range of flip angles, even though an RF pulse may have one intended role (e.g., refocusing), the pulse may make significant contributions in the other roles. For the purpose of our discussion, we will refer to the RF pulses in FSE imaging that follow the excitation RF pulse as refocusing RF pulses, even though, as described below, these RF pulses may also play the role of store/recall or excitation RF pulses for certain configurations of the pulse sequence.

SINGLE-SLAB 3D FAST SPIN ECHO

Increasing the Efficiency of Fast-Spin-Echo Imaging

Taking, as a starting point, the implementations of 2D FSE and multi-slab 3D FSE that existed in the 1990s, a considerable increase in efficiency was needed to make acquisition times for single-slab 3D FSE

clinically practical. Two basic strategies were used to achieve the necessary increase. First, modifications to the pulse-sequence structure were implemented to substantially increase the number of echoes (and, therefore, the number of lines of phase-encoding data) that can be acquired following each excitation RF pulse. These modifications included significantly shortening the echo spacing (7,87,88), and using variable-flip-angle refocusing RF pulses to suppress blurring (89,90) or to considerably lengthen the useable duration of the spin-echo train (91,92). New, flexible strategies for ordering the phase-encoding data in *k*-space were also necessary to take advantage of the longer echo-train lengths (93,94). Second, existing approaches for reducing the amount of *k*-space data required for image reconstruction were incorporated, including partial-Fourier acquisition (95,96) and parallel imaging (97,98). Advantages of partial-Fourier and parallel-imaging methods relevant to 3D-FSE acquisitions are discussed briefly in the section on phase-encoding strategies.

Shorter Echo Spacings

Most pulse sequences for clinical MRI use spatially selective (slice-selective) RF pulses, which are composed of a shaped RF waveform applied in the presence of a magnetic field gradient. These RF pulses typically have durations that range from approximately 1 ms up to roughly 10 ms, although those with a relatively short duration (~1 ms) are used only when a well-defined slice profile is not required. Because multi-slab 3D FSE requires a well-defined slice (slab) profile to minimize slab-boundary artifacts, slice-selective RF pulses for multi-slab 3D FSE typically have durations of at least a few milliseconds.

The timing diagram in Figure 5a shows one echo spacing from the echo train of a representative, multi-slab 3D-FSE pulse sequence. Specifically, the diagram shows two consecutive refocusing RF pulses and the associated gradient waveforms that are applied during and between the RF pulses; the excitation RF pulse is not shown. (See the figure caption for additional details.) In this example, the refocusing RF-pulse duration is 3.84 ms and the echo spacing is 8.5 ms; the RF pulse occupies 45% of the echo spacing. For comparison, Figure 5b shows the pulse-sequence diagram for single-slab 3D FSE over the same total time as Figure 5a. Because only a single slab is imaged, spatial selection is not required and therefore the spatially selective RF pulses, as shown in Figure 5a, can be replaced with short (0.6 ms in this example), non–spatially selective RF pulses that use a rectangular RF waveform to minimize pulse duration (7,87,88). (An analogous approach is used for certain 3D gradient-echo applications such as imaging the whole head or knee. Non–spatially selective refocusing RF pulses have also been used for 3D GRASE (GRadient- And Spin-Echo) imaging (99). Note, however, because spatial selection is not used, the thickness of the single slab, and thus the dimension of the spatially encoded volume along the slice-select direction, should encompass the entire extent of the object to prevent aliasing.) This permits the echo spacing to be reduced substantially, to 3.9 ms, and for this example the refocusing RF pulse occupies only 15% of the echo spacing. In general, if the desired receiver bandwidth is moderate to high (i.e., if the data sampling period is a few milliseconds in duration or shorter), then the use of short (< 1 ms), non–spatially selective refocusing RF pulses in place of conventional spatially selective RF pulses provides a significant reduction in the echo spacing, and permits, for a given echo-train duration, many more echoes to be collected following each excitation RF pulse.

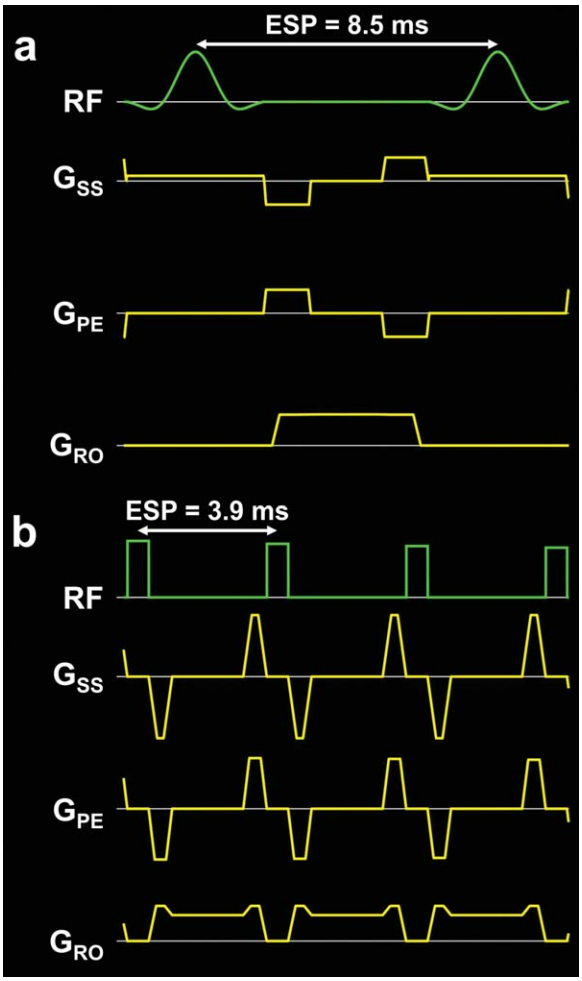

Figure 5. Shortening the echo spacing by using non–spatially selective refocusing RF pulses. Portions of the timing diagrams are shown for multi-slab (**a**) and single-slab (**b**) 3D-FSE pulse sequences to illustrate the difference between echo-spacing (ESP) values for the two techniques. The refocusing RF-pulse durations are 3.84 ms (spatially selective) and 0.6 ms (non–spatially selective) for the multi-slab and single-slab methods, respectively. The slice-select gradient for multi-slab 3D FSE has a low amplitude because the slab is relatively thick. For both pulse sequences, the in-plane (G_{PE}) and through-plane (G_{SS}) phase-encoding gradients overlap the spoiler (crusher) gradients applied along the readout axis; these spoiler gradients occur just before and just after data sampling. Both pulse sequences have a receiver bandwidth of 500 Hz/pixel and provide a spatial resolution of $1 \times 1 \times 1$ mm^3. (RF, radio frequency; G_{SS}, slice-select gradient; G_{PE}, in-plane phase-encoding gradient; G_{RO}, readout [frequency-encoding] gradient.)

An obvious difference between the general appearance of the gradient waveforms for multi-slab 3D FSE and that of the waveforms for single-slab 3D FSE deserves comment. Specifically, comparing the gradient waveforms in Figure 5a to those in Figure 5b, we see that both the in-plane (G_{PE}) and through-plane (G_{SS}) phase-encoding gradients for multi-slab 3D FSE are longer and lower in amplitude than those for single-slab 3D FSE. Similarly, for multi-slab 3D FSE, the spoiler [crusher] gradients on the readout axis, applied just before and just after data sampling, have an amplitude that is similar to that for the readout gradient itself, in contrast to the configuration for single-slab 3D FSE wherein the spoiler gradients are shorter and have an amplitude that is visibly higher. This situation arises because, for the multi-slab 3D-FSE example shown, the minimum time period that can be achieved between the centers of the excitation RF pulse (not shown in Fig. 5) and the first refocusing RF pulse is more than twice the minimum time period that can be achieved between successive refocusing RF pulses. Thus, the minimum echo spacing is determined by the former (minimum time period between excitation and first refocusing RF pulses) because this time period is, by definition, equal to one half of the echo spacing. The primary factor which results in this time period dictating the echo spacing is that the RF pulse durations (3.84 ms) are substantially longer than the data sampling period (2 ms). For the pulse sequence illustrated in Figure 5a, the phase-encoding and readout-spoiler gradient waveforms were configured to use the time available within the echo spacing, and thus, because the echo spacing is longer than the minimum value that could be achieved based on only the gradients applied between successive refocusing RF pulses, the waveforms can be made longer, thereby reducing the associated amplitudes. Nonetheless, even if the echo spacing for multi-slab 3D FSE was not constrained by the minimum time period achievable between the excitation and first refocusing RF pulses, the echo spacing for this example would remain more than 80% longer than that for single-slab 3D FSE.

Longer Echo Trains

The typical FSE pulse sequence (e.g., Fig. 1) uses relatively high flip angles for the refocusing RF pulses, generally equal to or at least near 180°. As we know, for a series of 180° refocusing RF pulses, all of the transverse magnetization created by the excitation RF pulse is refocused (Fig. 4b) at each echo time (assuming an ideal slice profile), and the signal decays during the echo train based on the T2 relaxation times of the tissues (e.g., Fig. 6a, center plot). For this circumstance, the echo-train duration used for clinical FSE imaging is typically less than the T2 values of primary interest for short TE_{eff} values (e.g., T1 or proton-density weighting), and less than two to three times these T2 values for long TE_{eff} values (e.g., T2 weighting). For example, the echo-train duration for T2-weighted FSE brain imaging is typically less than 300 ms because the T2 values for white matter and grey matter are approximately 100 ms at field strengths commonly used for clinical MRI (1.5T and 3T). Longer echo-train durations can result in degraded image contrast and artifacts such as blurring (78,100,101). Blurring occurs when the high spatial frequency data, which represents edge information in the image, is attenuated compared with data in the central region of *k*-space. Thus, when the echo-train duration is long relative to T2 values of interest, and the selected TE_{eff} value and phase-encoding order map the high spatial frequency data to the latter part of the echo train, for which the echo amplitudes are substantially attenuated due to T2 decay, edges in the image appear blurred.

Over 20 years ago, Hennig proposed the use of constant low-flip-angle refocusing RF pulses to introduce T1 dependence to the evolution of the echo train and thereby lengthen its useable duration for biological tissues, which generally have T1 values that are much longer than their T2 values (102). The result of using relatively low flip angles for the refocusing RF pulses in FSE is seen by comparing the plots in Figure 6b (constant 60° flip angles for the refocusing RF pulses) to those in Figure 6a (constant 180° flip angles). The plots in the center column of Figure 6 show the signal evolutions that result from the corresponding flip angle values in the left column for a fairly long echo train—200 echoes with a spacing of 4 ms between echoes—and a tissue with representative relaxation times (T1/T2 1000/100 ms). For echo times greater than approximately 200 ms, we see that the signal for constant 60° flip angles is greater than that for constant 180° flip angles. This is because the 60° refocusing RF pulses generate both spin echoes and stimulated echoes (Fig. 4b,c). Recall, as discussed above, that during the "storage period" for the stimulated echo (Fig. 3g,h) the magnetization, which later forms the echo, decays according to the T1 relaxation time of the tissue. Because T1 is 10 times longer than T2 for our example, the stimulated-echo contribution to the total signal permits higher signal amplitudes for relatively long echo times.

The plots in the right column of Figure 6 show two quantities that are useful for assessing the overall performance of the refocusing RF pulses; these quantities are generated based on the magnetization components within a voxel that are associated with regions experiencing different resonance frequencies, such as depicted in Figure 3 by red and green vectors. At each echo time, the dashed lines depict the fraction of the magnetization, originally generated by the excitation RF pulse, which is currently aligned with the z-axis. In terms of our description above for stimulated echoes, this is the fraction of magnetization "stored" along the z-axis. Because 180° RF pulses refocus all of the transverse magnetization created by the excitation RF pulse (Fig. 4b), this quantity is zero throughout the echo train for this case (Fig. 6a, right plot). In contrast, and as expected, the fraction of magnetization stored along the z-axis is significant for 60° refocusing RF pulses (Fig. 6b, right plot). As noted in the preceding paragraph, it is the existence of this stored component, which decays with T1, that allows higher signal amplitudes to be achieved for relatively long echo times (Fig.

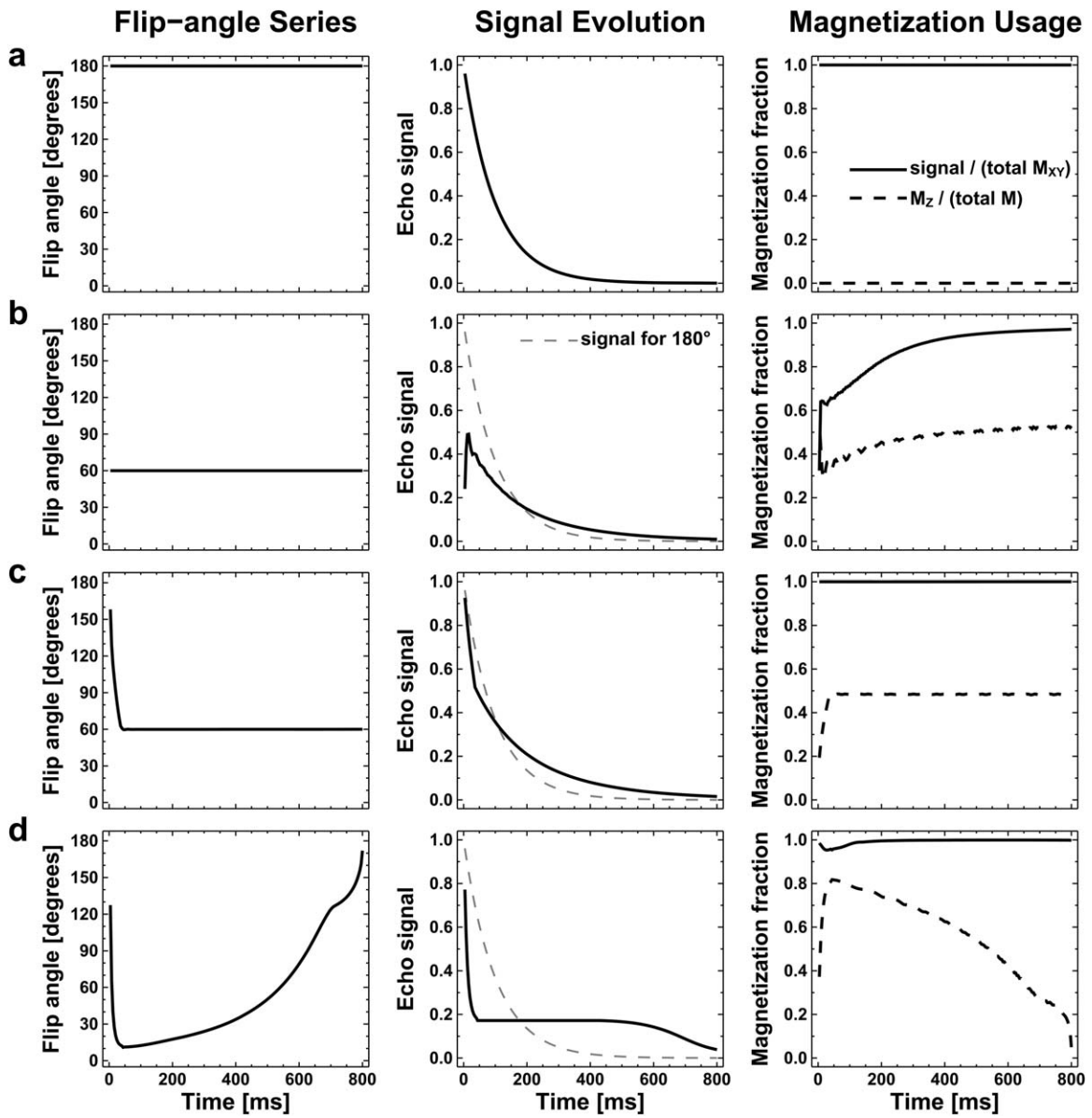

Figure 6. Lengthening echo-train duration by using variable flip angles for the refocusing RF pulses. For four flip-angle scenarios, the plots show the flip angles for the refocusing RF pulses (left column), the associated echo-signal amplitudes (center column), the fraction of magnetization in the transverse plane that generates signal (right column, solid line), and the fraction of magnetization stored along the *z*-axis (right column, dashed line) during an 800-ms echo train. The flip-angle scenarios include constant 180° refocusing RF pulses (**a**), constant 60° refocusing RF pulses (**b**), an initial flip-angle ramp followed by constant 60° refocusing RF pulses (**c**), and flip angles that vary throughout the echo train (**d**). Refocusing-RF-pulse flip angles less than 180° (b–d), which generate an echo train containing both spin echoes and stimulated echoes, provide increased signal amplitudes at relatively long echo times because T1 is longer than T2. Appropriate variation of the flip-angle values during the echo train (c,d) optimizes usage of the available magnetization, yielding signal amplitudes during the central portion of the echo train that are higher than those obtained for constant 180° refocusing RF pulses. (Echo-train length, 200; echo spacing, 4 ms; T1/T2, 1000/100 ms; repetition time long relative to T1; M, magnetization; M_{XY}, transverse magnetization; M_Z, longitudinal [*z*-axis] magnetization.)

6b, center plot). The solid lines for the plots in the right column of Figure 6 depict the fraction of the magnetization in the transverse plane that generates signal. (For example, Fig. 3j illustrates the situation wherein the signal [echo amplitude] is less than the maximum possible value for the existing transverse magnetization. At the time of the stimulated echo, the transverse magnetization vectors are not aligned along a common axis, and thus the echo amplitude is less than the value which would be obtained if the vectors were all aligned.) This quantity indicates how efficiently the available transverse magnetization is used by the pulse sequence. Although constant 60° refocusing RF pulses provide signal at long echo times that is higher than the signal from constant 180° refocusing RF pulses, we see in the right plot of Figure 6b that the transverse magnetization is not used very efficiently. Specifically, the values for the solid curve never reach 1, and are less than 0.8 for the first quarter of the echo train. Finally, another undesirable characteristic of the signal

evolution for constant 60° refocusing RF pulses is the rapid oscillation in signal amplitude that occurs at the beginning of the echo train as the magnetization splits among various spin-echo and stimulated-echo pathways. The large jump in signal amplitude between the first and second echoes occurs because the first stimulated echo is formed following the second refocusing RF pulse, and adds to the associated spin echo. For 60° refocusing RF pulses, the first stimulated echo is more than 6 times larger than the (second) spin echo, causing the signal amplitude of the second echo to be much larger than even that of the first echo.

In the late 1990s Alsop described an approach for improving the behavior of echo trains that use primarily constant-flip-angle refocusing RF pulses and flip-angle values less than 180° (103). As illustrated in Figure 6c, if the flip-angle values are ramped down at the beginning of the echo train, from a relatively high value to the constant value used for the majority of the echo train, then the general behavior of the signal evolution is improved and the signal amplitudes achieved at long echo times are increased. Comparing the right plot for Figure 6c to that for Figure 6b, we see that, with the flip-angle ramp, the pulse sequence makes very efficient use of the available transverse magnetization (i.e., the solid line in Fig. 6c, right plot, is close to 1 for all echo times). In addition, the initial rapid oscillation in signal amplitude, which occurs for constant 60° refocusing RF pulses, is eliminated. This flip-angle scheme (initial flip-angle ramp followed by constant flip-angle values) is useful for several applications of single-slab 3D FSE.

A further substantial improvement in the signal evolution can be made by appropriately varying the flip-angle values throughout the echo train, as illustrated by the example shown in Figure 6d. In particular, we see that the signal amplitudes for echo times in the central portion of the echo train are much higher than those for constant 180° flip angles. At the midpoint (400 ms), the signal amplitude is approximately 10 times higher than that for constant 180° flip angles. Insight into how the variable-flip-angle series achieves this desirable signal behavior is provided by examining the fraction of magnetization stored along the z-axis during the echo train (dashed line in Fig. 6d, right plot). The initial portion of the variable-flip-angle series stores a large fraction (up to ~80%) of the magnetization along the z-axis. Then, as the echo train proceeds, this stored magnetization is gradually converted to transverse magnetization, permitting relatively high signal amplitudes to be maintained for the central portion of the echo train. The variable-flip-angle series also makes efficient use of the available transverse magnetization; the solid line in Figure 6d, right plot, is near 1 throughout the echo train.

The utility of the variable-flip-angle approach for extending the useable duration of the echo train is illustrated in Figure 7 for T2-weighted FSE imaging of the brain. In this figure, the result for constant high flip angles (170°) is compared with that for variable flip angles when a 660-ms, 160-echo train is used. For constant high flip angles, the image contrast is strongly T2 weighted, as expected; cerebrospinal fluid appears bright while brain white matter and grey matter appear quite dark. In contrast, with variable flip angles, brain white matter and grey matter are no longer dark, and the overall image contrast appears essentially the same as that for a conventional T2-weighted image with an echo time of roughly 100 ms.

Historically, the development of variable-flip-angle approaches for spin-echo train imaging focused on two main goals: suppressing blurring (89,90), or considerably lengthening the useable duration of the spin-echo train (91,92). In 1994, Schäffter et al (89) described the use of variable-flip-angle refocusing RF pulses to suppress blurring in single-shot GRASE imaging. Later, in 1999, Mugler et al (90) demonstrated single-slab 3D FSE with variable-flip-angle refocusing RF pulses to suppress blurring for proton-density-weighted or T1-weighted imaging, and, in the following year (91), described single-slab 3D FSE with variable-flip-angle refocusing RF pulses to substantially lengthen the echo-train duration for T2-weighted imaging. Subsequently, several research teams have developed optimizations for variable-flip-angle calculations and applications to 3D-FSE imaging (92,93,104–108).

The reader may wonder how the hyperecho/TRAPS variable-flip-angle schemes described by Hennig et al (109,110) fit into single-slab 3D-FSE imaging. Recall that the hyperecho concept describes the manner in which the flip and phase angles of the refocusing RF pulses in a spin-echo train can be varied along the echo train to yield full refocusing (neglecting relaxation) of the initially excited magnetization as a "hyperecho" (109). TRAPS (TRAnsition between Pseudo-steady States) is a special case of the hyperecho concept and has been applied for reduction of power deposition in 2D-FSE imaging (110,111), although these specific TRAPS flip-angle schemes are suboptimal for substantially lengthening the echo-train duration for tissues such as brain grey matter because the central flip-

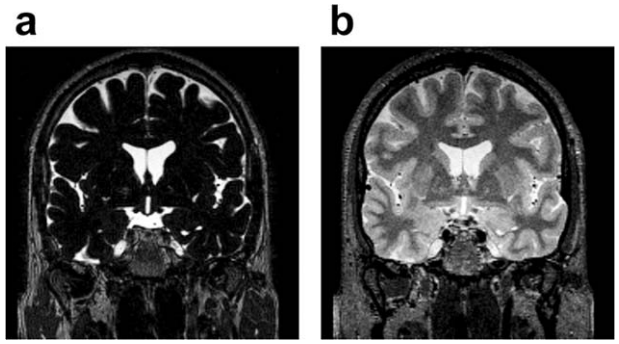

Figure 7. Utility of variable-flip-angle refocusing RF pulses for extending the useable duration of the echo train in 3D-FSE imaging. Coronal brain MR images are shown from a healthy volunteer (TR/TE_{eff}, 2750/330 ms; 660-ms, 160-echo train; 1.5T). **a:** Constant 170° refocusing RF pulses yield strong T2 weighting, with relatively low signal intensities for brain white matter and grey matter. **b:** Variable-flip-angle refocusing RF pulses yield substantially increased signal intensities for white matter and grey matter, and image contrast comparable to that for a conventional T2-weighted FSE image with TE_{eff} of approximately 100 ms.

angle value is 180°. Nonetheless, the hyperecho/TRAPS concepts are particularly valuable for understanding the fundamental behavior of variable-flip-angle approaches appropriate for single-slab 3D FSE, and the TRAPS formalism is applicable to deriving variable-flip-angle series suitable for single-slab 3D FSE, as discussed by Busse et al (93). Nonetheless, and contrary to some published accounts of the development of single-slab 3D FSE (112), variable-flip-angle schemes for single-slab 3D-FSE imaging were developed and experimentally demonstrated (90,91) before introduction of hyperecho/TRAPS concepts.

Efficient Phase-Encoding Strategies

Established phase-encoding methods for 2D- and multi-slab 3D-FSE imaging are based on placing the data from a given echo train into a single plane of *k*-space. Thus, for the 3D case, a given echo train typically acquires data associated with a single value of the through-plane phase-encoding gradient. With the efficiency improvements described above, single-slab 3D FSE can easily generate a sufficient number of echoes following each excitation RF pulse to fill a large portion of a single plane of *k*-space, and, in some instances, can yield enough data to fill multiple planes of *k*-space. The established (single *k*-space plane) methods cannot effectively use this relatively large amount of data from each echo train, and thus dedicated phase-encoding schemes for single-slab 3D FSE are required.

In an initial attempt to address this problem, a scheme was proposed to distribute the data from a given echo train along the in-plane phase-encoding direction, analogous to established 2D-FSE methods, and also across a small number of *k*-space planes corresponding to the through-plane phase-encoding direction (113). The number of planes used in the through-plane phase-encoding direction was termed the "slice turbo factor." Although this method improves usage of the data from long echo trains, it imposes an undesirable limitation on the relationship between echo-train length and image matrix size because the numbers of echoes from a given echo train placed in each *k*-space plane are constrained to be equal.

Subsequently, more efficient phase-encoding schemes for single-slab 3D FSE were developed by discarding requirements regarding the number of echoes placed in a given plane of *k*-space (93,94). By determining an optimum distribution in *k*-space for each echo train, given the echo-train length, desired contrast properties, and image matrix size, essentially all of the data can be used and the image matrix size can be selected independent of the echo-train length.

Examples of efficient phase-encoding ordering for single-slab 3D FSE, described by Busse et al (93), are shown in Figure 8. For each plot, the horizontal axis corresponds to the position in *k*-space along the in-plane phase-encoding direction (the center of *k*-space is at index 50) and the vertical axis corresponds to the position in *k*-space along the through-plane phase-encoding direction (the center of *k*-space is at index 40). This example assumes "elliptical" sampling of *k*-space, that is, the "corners" of *k*-space are not sampled. The plots in the left column illustrate how data from the echo trains are sorted with respect to echo number to achieve the desired contrast for a long TE_{eff} (Fig. 8a) or short TE_{eff} (Fig. 8c). For a long TE_{eff}, the echo numbers are mapping along the in-plane phase-encoding direction in sequential order such that the echo midway along each echo train corresponds to the central region of *k*-space (Fig. 8a). Note that a given echo number may be associated with more than one plane of *k*-space; for example, "echo 1" in Figure 8a is mapped to three adjacent planes. This permits efficient use of the available data. For a short TE_{eff}, the echo numbers are mapped in a radial manner such that low echo numbers (short echo times) are in the central region of *k*-space, and the echo number increases with distance from the center of *k*-space (Fig. 8c). Although, ideally, a given echo number would be mapped to a specific radius, in practice the radius value is allowed to vary over a small range (e.g., see placement of "echo 15" in Fig. 8c) to permit efficient use of the available data.

The plots in the right column of Figure 8 illustrate how data from given echo trains are mapped into *k*-space to achieve a long TE_{eff} (Fig. 8b) or short TE_{eff} (Fig. 8d). In analogy to the scheme for data placement based on echo number, a given echo train is not constrained to fall within a single *k*-space plane (Fig. 8b), or at a single angular value with respect to the center of *k*-space (Fig. 8d), but instead is mapped to a small range of planes or angular values to permit efficient use of the available data while maintaining image quality as determined by the *k*-space filter imposed by variation of signal amplitude along the echo train (93).

Because two dimensions are phase encoded in a 3D acquisition, as compared to one in a 2D acquisition, 3D methods provide the opportunity for higher acceleration using parallel imaging. For example, the two cases shown in Figure 8 include parallel imaging for both phase-encoding directions, providing a multiplicative decrease in imaging time. The region in the central portion of each plot, showing more closely spaced dots, represents full sampling in *k*-space to obtain calibration data for the parallel-imaging reconstruction. Outside of the central region, *k*-space is undersampled by a factor of two along each direction, providing a factor of four (2×2) parallel-imaging acceleration. In this respect, the flexible phase-encoding scheme is important because it permits the region of full sampling to include only the required data. Parallel-imaging acceleration in two dimensions in conjunction with traditional phase-encoding schemes results in acquisition of unnecessary data, thus decreasing scan efficiency. See Figure 2 and associated text in Busse et al (93) for additional details.

Partial-Fourier sampling, wherein a portion of the high spatial frequency data is not collected, provides another means to accelerate the acquisition (95,96). For example, the short TE_{eff} example (Fig. 8c,d) shows data along the in-plane phase-encoding direction only for indices 0 through 60 because partial-Fourier sampling (as well as parallel-imaging) is used along the

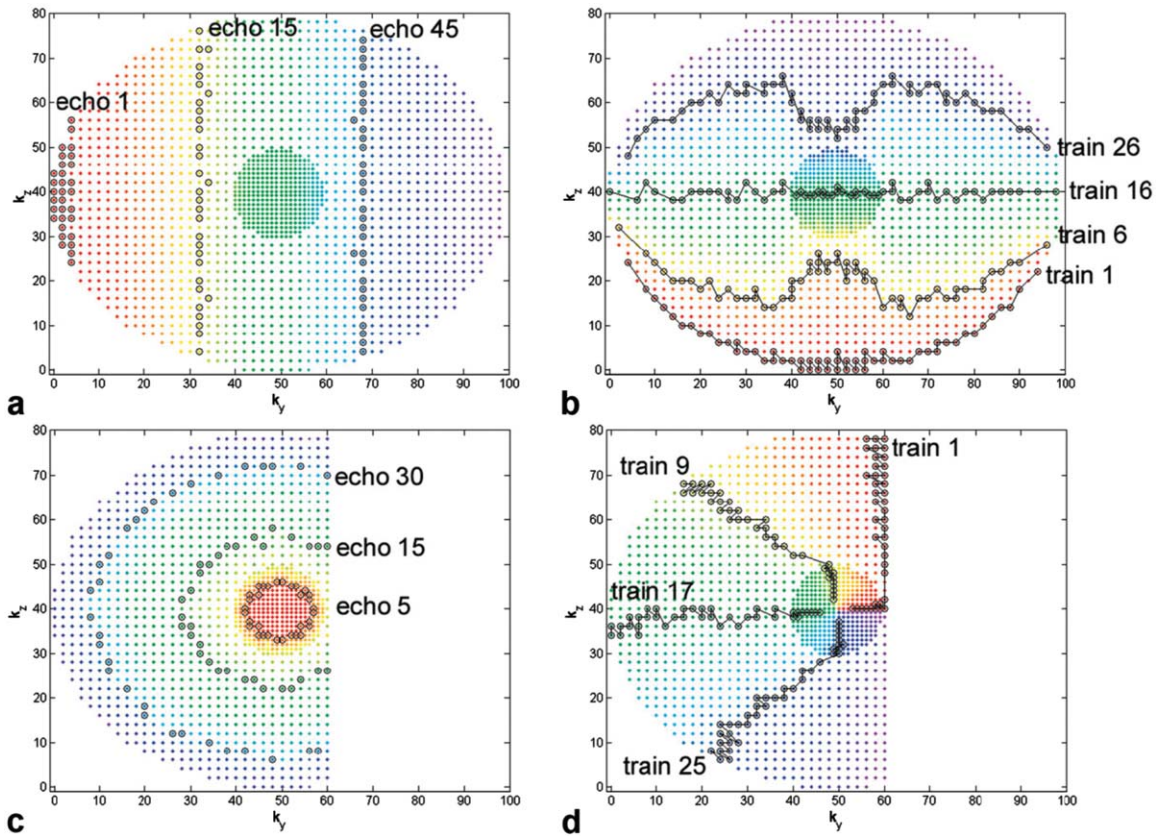

Figure 8. Efficient phase-encoding strategies for single-slab 3D FSE. The plots illustrate how data are mapped into *k*-space along the in-plane (labeled k_y) and through-plane (labeled k_z) phase-encoding directions to achieve long (**a**,**b**) or short (**c**,**d**) TE_{eff} values for an acquisition based on 100 (in-plane) × 80 (through-plane) phase-encoding steps. Each colored dot represents one echo from a spin-echo train. The plots in the left column show the data sorting with respect to echo number to achieve the desired contrast. Linear, sequential ordering is used to obtain a long TE_{eff} value (a), and radial ordering is used to obtain a short TE_{eff} value (c). The plots in the right column show how data for selected echo trains are mapped into *k*-space. The long and short TE_{eff} examples include elliptical sampling of *k*-space, and parallel-imaging acceleration (factor of 2) along both phase-encoding directions; the round central region in each plot with full data sampling represents the calibration data for parallel-imaging reconstruction. The short TE_{eff} example also includes partial-Fourier sampling along the in-plane phase-encoding direction, and thus no data samples are shown for indices greater than 60. (Fig. 3 from Ref. (93), reproduced with permission.)

in-plane phase-encoding direction to further decrease acquisition time. Analogous to conventional FSE imaging, partial-Fourier sampling is particularly useful in 3D FSE for applications requiring moderate to short TE_{eff} values (93,107).

Contrast Behavior: Effect of Refocusing Flip Angles

The relationship between the contrast behavior for single-slab 3D FSE and that for conventional 2D FSE depends on the flip-angle values used for the refocusing RF pulses. Currently, the flip-angle schemes typically used for single-slab 3D FSE can be divided into three main categories: (1) relatively high, constant flip angles; (2) a short to moderate TE_{eff} value and variable flip angles (including values substantially less than 180°) or an initial flip-angle ramp followed by relatively low, constant flip angles; and (3) a long TE_{eff} value and variable flip angles (including values substantially less than 180°) or an initial flip-angle ramp followed by relatively low, constant flip angles. (If the constant flip angle used for category 1 is less than 180°, an initial variable-flip-angle ramp is often included, although this is not critical in the context of our current discussion.)

The contrast behavior for single-slab 3D FSE using relatively high, constant flip angles for the refocusing RF pulses (category 1) is essentially the same as that for 2D FSE using similar flip-angle values. Nonetheless, there are some factors that may lead to subtle contrast differences between the two techniques. For example, the flip angle for any given slice from a single-slab 3D-FSE acquisition is constant in the slice-select direction (aside from any effect of transmit-B1 inhomogeneity), while, depending on the quality of the slice profile for the refocusing RF pulses, the flip angle may vary substantially across the slice for 2D-FSE imaging. Depending on the degree of this flip-angle variation across the slice, TR and TE_{eff} values, echo-train length, and relaxation times, minor differences in contrast may be apparent even when the nominal flip-angle values for the two techniques are the same. Another potential source of minor contrast differences

is magnetization transfer effects. Because the 3D-FSE acquisition includes only one (thick) slice, RF pulses associated with a given slice do not act as off-resonance RF pulses for other slices, as in multi-slice 2D-FSE imaging (83).

When at least some of the refocusing RF pulses have relatively low flip-angle values (categories 2 and 3), the contrast developed at TE_{eff} (echo time corresponding to the center of *k*-space) may be much different than that for 180° refocusing RF pulses (91), and depends both on TE_{eff} and the values of the refocusing-RF-pulse flip angles preceding TE_{eff} (92,109–111). As discussed above in the section on *Longer Echo Trains*, a portion of the magnetization generated by the excitation RF pulse is stored along the z-axis during the echo train for refocusing-RF-pulse flip angles less than 180° (Fig. 6b–d, right column), and the associated signal evolution is composed of both spin echoes and stimulated echoes. Thus, at TE_{eff}, some of the magnetization contributing to the signal will have spent a fraction of TE_{eff} stored along the z-axis, during which time this magnetization decays based on T1; the fraction of time this magnetization spends in the transverse plane, subject to T2 decay, is therefore reduced. As a result, the contribution of T2 decay to the signal amplitude at TE_{eff} is less than that which would have occurred for 180° refocusing RF pulses, and the apparent echo time for the corresponding image, which reflects the contrast seen among tissues in the image, is less than TE_{eff}. This effect is clearly seen in the brain image shown in Figure 7b; the TE_{eff} value is 330 ms, but the image contrast appears consistent with an echo time of approximately 100 ms.

Fortunately, the effect of stimulated echoes on the image contrast can be calculated, and, when flip angles less than 180° are used for the refocusing RF pulses, the echo time which reflects image contrast can be explicitly determined (92,109–111), as discussed with the introduction of hyperechoes by Hennig and Scheffler (109). The sagittal brain images in Figure 9, from single-slab 3D-FSE acquisitions using variable and constant-180° flip angles, illustrate this concept (92). The image in Figure 9a, acquired using variable-flip-angle refocusing RF pulses, has a TE_{eff} (center of *k*-space) value of 585 ms, whereas the echo time calculated to predict the image contrast is 140 ms (92). For comparison, Figure 9b and 9c show images acquired using constant-180° flip angles with TE_{eff} values of 585 ms and 140 ms, respectively. While, the image in Figure 9b shows heavily T2-weighted contrast, as expected, the image in Figure 9c demonstrates contrast substantially the same as that for the image in Figure 9a, confirming that the calculated "contrast-equivalent" echo time reflects the image contrast for the variable-flip-angle 3D-FSE acquisition. When the TE_{eff} value is relatively short (category 2), the flip-angle values for the refocusing RF pulses have a relatively minor effect on the contrast developed at TE_{eff}, and thus the contrast-equivalent echo time and TE_{eff} value will be similar, unlike the case for long TE_{eff} values (category 3). The principle of calculating a corrected echo-time value which reflects equivalent contrast to an acquisition using constant-180° flip angles has also been applied to TRAPS variable-flip-angle schemes for 2D-FSE imaging, as described by Weigel and Hennig (111).

For 3D-FSE imaging with variable or relatively low flip angles, a source of potential confusion is the fact that the echo time which reflects image contrast may be quite different than that which corresponds to the center of *k*-space. Herein, we consistently use TE_{eff} to denote the echo time corresponding to the center of *k*-space, in agreement with its usage for 2D-FSE imaging. Nonetheless, in the literature, some authors have used the term effective echo time to denote the echo time which reflects image contrast for a variable or low flip-angle 3D-FSE pulse sequence, without direct reference to the echo time at which the center of *k*-space is acquired (23). Both echo-time values are important for describing the behavior and structure of the pulse sequence. Hopefully, manufacturers will adapt a consistent nomenclature for 3D-FSE imaging in the future so that the important aspects of these

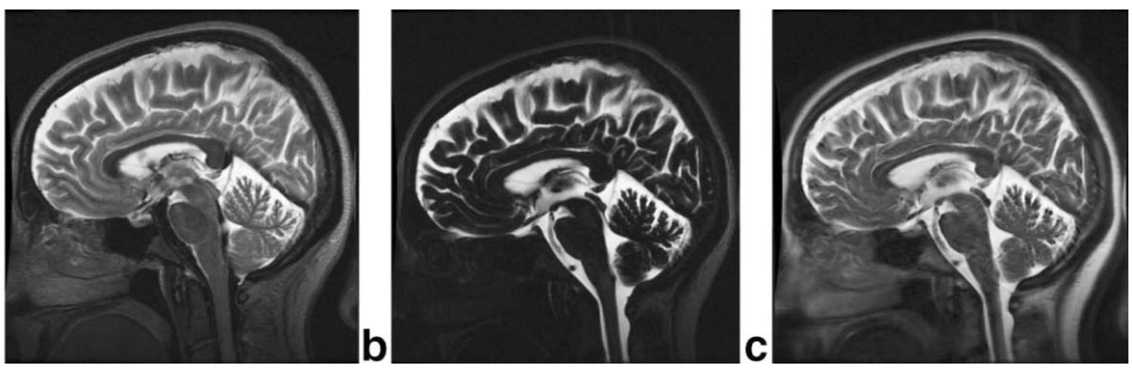

Figure 9. Contrast behavior for a variable-flip-angle 3D-FSE acquisition. Sagittal brain images (TR 2500 ms) are shown from single-slab 3D-FSE acquisitions using variable-flip-angle refocusing RF pulses and a TE_{eff} value of 585 ms (**a**), or constant 180° refocusing RF pulses and a TE_{eff} value of 585 ms (**b**) or 140 ms (**c**). The "contrast-equivalent" echo time for image (a) is calculated to be 140 ms (92), and the contrast for the image is essentially the same as that for image (c), for which TE_{eff} is 140 ms. In image (a), the substantial reduction of signal intensity for cerebral spinal fluid surrounding the midbrain and cervical spine is due to motion sensitivity introduced by the low flip-angle values used in the variable-flip-angle series (67,93,125). (Fig. 6 from Ref. (92), reproduced with permission.)

pulse sequences can be clearly conveyed. In the meantime, the reader should be aware that, in the literature or on an MR scanner interface, the stated effective echo time may refer either to image contrast or to the center of *k*-space.

As noted in the background section on *2D Fast-spin-echo Imaging*, there can be subtle contrast differences between conventional spin-echo and 2D FSE even when the TE value for spin echo matches the TE_{eff} value for fast spin echo. Similarly, subtle contrast differences between 2D FSE and variable or low flip-angle 3D FSE may be expected even when the TE_{eff} value for 2D FSE matches the contrast-equivalent TE for 3D FSE.

Power Deposition

The power deposition (SAR, specific absorption rate) for an RF pulse using a given waveform shape varies as the square of the amplitude of the pulse, and, for amplitude-modulated RF pulses as commonly used for clinical MRI, the flip angle is directly proportional to the pulse's amplitude. Thus, SAR varies as the square of the flip angle for the RF pulse. For clinical FSE imaging, this relationship is often used to meet regulatory power-deposition limits by reducing the flip angle for the refocusing RF pulses somewhat below 180°. For example, a flip-angle decrease from 180° to 150° reduces SAR by over 30%. It is thus no surprise that variable-flip-angle refocusing RF pulses offer the opportunity for substantial SAR reduction in spin-echo-train imaging compared with conventional, high-flip-angle refocusing RF pulses. This possibility was postulated for GRASE imaging at least as early as 1994 (89).

Consider, for example, the four flip-angle scenarios shown in Figure 6. If we assume a normalized SAR value of 100% for the case of constant 180° flip angles, the corresponding normalized SAR values are 11%, 12% and 15% for constant 60° flip angles, an initial flip-angle ramp followed by constant 60° flip angles, and flip angles that vary throughout the echo train, respectively. Thus, compared with constant 180° flip angles, the variable-flip-angle series of Figure 6d provides an order of magnitude greater signal amplitude midway through the echo train, while depositing roughly seven times less power. As a second example, the local SAR values reported by the MR scanner for the subject of Figure 7 were 5.23 W/kg for constant 170° flip angles and 0.88 W/kg for the variable-flip-angle refocusing RF pulses—a sixfold reduction for the variable-flip-angle series.

Early in the development of single-slab 3D FSE with variable-flip-angle refocusing RF pulses, researchers explored the potential benefits of SAR reduction for high-field imaging. Mugler et al found that T2-weighted whole-brain imaging at 3T with variable-flip-angle 3D FSE yielded power-deposition well below regulatory (FDA) limits (114). More recently, Sarkar et al described T2-weighted and FLAIR single-slab 3D-FSE pulse sequences for brain imaging at 1.5T that yield whole-body SAR values roughly 100 times below the regulatory limit (23). This very low power deposition was achieved by optimization of the variable-flip-angle values, particularly those for the latter half of the echo train, and by increasing the duration of the RF pulses, which in turn lowers the pulse amplitude for a given flip-angle value. Although these pulse sequences were demonstrated at 1.5T, the power deposition should be sufficiently low to permit operation at any field strength currently used for human imaging, including 7T.

Practical Issues and Artifacts

Signal Evolutions for Variable Flip Angles

The signal evolution shown in Figure 6d (center column) illustrates that it is possible to use variable-flip-angle refocusing RF pulses to achieve uniform signal amplitude over a substantial portion of a long spin-echo train. Nonetheless, the specific signal-evolution shape depends on the relaxation times for the tissue, and thus the shape will be somewhat different for other relaxation times. Figure 10a shows the flip-angle series and signal evolution from Figure 6d, for which the relaxation times approximate those for brain grey matter at 1.5T, and in addition includes the signal evolution for relaxation times representative of those for brain white matter at 1.5T (T1/T2 700/90 ms; dashed line). The overall shape of the signal evolution for white matter is only slightly different than that for grey matter. The echo-train parameters used for Figure 10a are applicable to T2-weighted imaging, wherein TE_{eff} (center of *k*-space) is within the central portion of the echo train. For this case, the point spread functions associated with the two signal evolutions are very similar, and hence there would not be significant degradation in image quality due to differences between the signal evolutions for the two tissues. (Because the initial signal ramp, which includes signal amplitudes that are much higher than those in the remainder of the signal evolution, occurs over only the first few echoes of the train, the associated data could be discarded, if desired, with only minor loss of efficiency.) Thus, although the signal-evolution shapes for variable-flip-angle refocusing RF pulses depend on the relaxation times, the evolution shapes will generally be similar across a range of tissue types unless the variation in relaxation times among tissues is very large.

Variable-flip-angle refocusing RF pulses offer a tremendous range of possibilities for 3D-FSE imaging. For example, Figure 10b shows the flip-angle series that yields uniform signal amplitude throughout the echo train for relaxation times approximating those for brain grey matter at 1.5T. These echo-train parameters could be used in conjunction with a very short TE_{eff} value. For this case, the signal evolution for brain white matter (dashed line) would yield some blurring because the signal amplitudes decrease monotonically as the echo train proceeds, although the blurring would be minor because the final signal amplitude for white matter is only approximately 15% less than that for grey matter. Examples of various signal evolutions obtained using variable-flip-angle

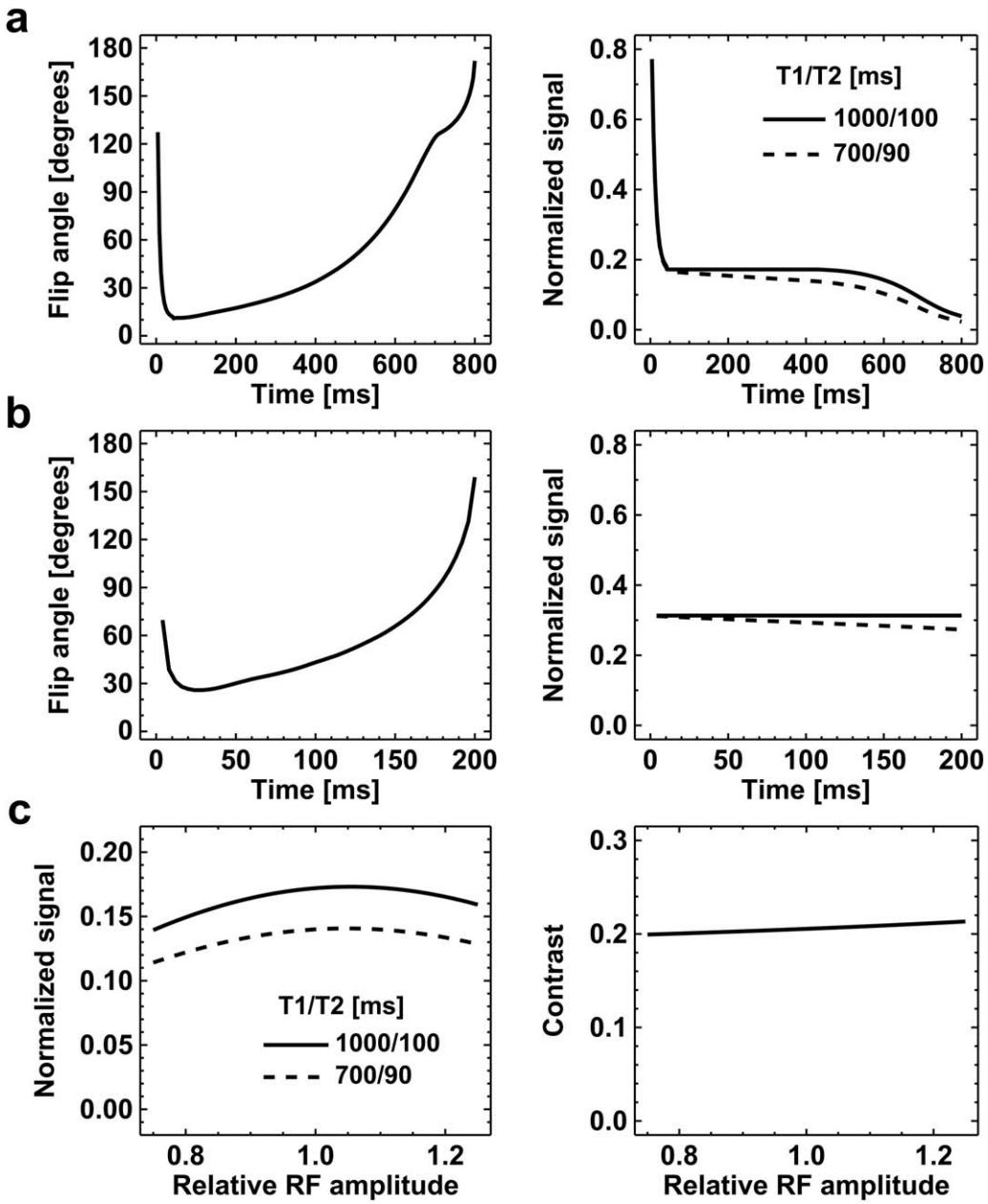

Figure 10. Signal evolutions for variable-flip-angle refocusing RF pulses. **a:** For the same variable-flip-angle series as shown in Figure 6d (left column), the plot on the right compares the echo-signal evolutions for relaxation times approximating those for brain grey matter (T1/T2, 1000/100 ms; solid line) and brain white matter (T1/T2, 700/90 ms; dashed line) at 1.5T. **b:** The variable-flip-angle series shown on the left yields uniform echo-signal amplitudes throughout the 200-ms echo train for relaxation times approximating those for brain grey matter at 1.5T. For both (a) and (b), the signal-evolution shape shows only a weak dependence on relaxation times. **c:** Signal (left plot) and contrast (right plot) at the center of the echo train for the variable-flip-angle series and two tissues considered in (a), as the RF amplitude is varied from −25% to +25% of the intended value. The contrast (signal difference divided by mean signal) shows only a weak dependence on RF amplitude. (Echo-train length, 200 for (a) and (c), and 50 for (b); echo spacing, 4 ms; repetition time long relative to T1; proton density difference between grey matter and white matter neglected.)

refocusing RF pulses can be found in references (23,89–93,104,107,108,110). It is reasonable to expect that improved variable-flip-angle series and associated signal evolutions will be developed for specific applications in the future.

Another important practical consideration for signal evolutions from variable-flip-angle refocusing RF pulses is the homogeneity of transmitted RF-field. As noted above in the section on Power Deposition, the flip angle for amplitude-modulated RF pulses, as commonly used for clinical MRI, is directly proportional to the pulse's amplitude. Thus, variation of the transmitted RF-field across the volume of interest translates directly to variation of the flip angle. RF-field homogeneity becomes a significant issue when the RF wavelength is similar to or smaller than the dimensions of

the object being imaged; clinically, this translates to magnetic field strengths of 3T or higher. Fortunately, signal evolutions from variable-flip-angle refocusing RF pulses do not typically degrade rapidly as the flip angles deviate from their intended values. Figure 10c presents an example based on the flip-angle series and signal evolutions of Figure 10a. The left plot in Figure 10c shows the signal amplitude from the two tissues, at the center of the echo train, as the RF amplitude varies from −25% to +25% of the intended value. (A relative RF amplitude of 1.0 corresponds to applying the intended flip-angle values as shown in Fig. 10a, left plot.) The signals slowly and smoothly decrease as the RF amplitude (flip angle) deviates from the ideal value of 1.0. The right plot shows how the corresponding contrast (difference between signals divided by mean of the signals) at the center of the echo train changes as the RF amplitude is varied. Because the signal curves for the two tissues approximately track one another, the relative change in contrast is less than that in the signal amplitudes; the contrast varies less 10% across the range of RF amplitudes considered. A larger variation in RF amplitude than that considered here may be encountered in practice, particularly at very high field strengths. Additional research is needed to better characterize and optimize variable-flip-angle refocusing RF pulses under conditions of substantial RF-field inhomogeneity.

FID Artifacts

In previous sections, we described the utility of variable-flip-angle refocusing RF pulses for extending the echo-train duration and reducing power deposition. However, like many things in MRI, the advantages of variable-flip-angle refocusing RF pulses also come with a potential problem—free-induction-decay (FID) artifacts. As illustrated in Figure 4, an RF pulse with an intermediate flip-angle value plays three roles: excitation (to generate transverse magnetization), refocusing (to generate a spin-echo), and store/recall (to generate a stimulated echo). Thus, if the flip angles of the refocusing RF pulses are not equal to 180°, longitudinal magnetization that regrows due to T1 relaxation during the time period between the excitation and first refocusing RF pulses, or between successive refocusing RF pulses, will be converted to transverse magnetization by the next refocusing RF pulse that is applied, and thereby create an FID signal. Nonetheless, when the flip-angle values for the refocusing RF pulses are relatively high (i.e., close to 180°), the associated FID signals are relatively small for the following two reasons. First, as shown in Figure 4a, the fraction of magnetization excited by an RF pulse having a flip angle close to 180° is quite small. Second, any longitudinal magnetization that regrows following an RF pulse will be very nearly inverted by the next RF pulse if the associated flip-angle value is close to 180°. As a result, the longitudinal magnetization has to then regrow from a starting point along the negative z-axis, and the amplitude of the longitudinal magnetization before any given refocusing RF pulse never becomes large. In contrast, when the flip-angle values for the refocusing RF pulses are relatively low, the refocusing RF pulse can convert a large fraction of the longitudinal magnetization that exists just before the RF pulse to transverse magnetization, and the amplitude of the longitudinal magnetization that exists before any given refocusing RF pulse can grow to become relatively large if the T1 relaxation time associated with the tissue is short compared with the duration of the echo train. If, however, the T1 relaxation time is long compared with the duration of the echo train, then regrowth of magnetization during the echo train will not result in large FID signals even when the flip-angle values for the refocusing RF pulses are relatively low.

Figure 11 illustrates concepts described in the preceding paragraph. This figure plots the amplitude of the FID signals generated by a train of refocusing RF pulses for the same echo-train length and echo spacing as those used for Figure 6. Because the FID signals increase with decreasing T1, relatively short relaxation times (T1/T2 300/60 ms, representative of fat at 1.5T) were used to generate the curves shown in Figure 11, demonstrating one of the worst cases in practice. For refocusing RF pulses having a constant flip angle of 180° (as used in Fig. 6a), the FID signals are zero throughout the echo train, as expected, because an RF pulse with a flip angle of 180° does not convert longitudinal magnetization to transverse magnetization (Fig. 4a). When the flip angle is decreased from 180° to 160°, FID signals are generated by the refocusing RF pulses, however the signal amplitudes are relatively small (Fig. 11, dashed line) for the reasons discussed above. Conversely, with variable-flip-angle refocusing RF pulses (same values as used in Fig. 6d), the signal amplitudes are relatively large (Fig. 11, solid line). The maximum value for variable flip angles is more than ten times greater than that for constant 160° flip angles. Furthermore, the amplitudes of the FID signals during the latter portion of the echo train are comparable to the echo signals shown in Figure 6d (compare solid line to Fig. 6d, center column).

An example of the artifact generated in single-slab 3D FSE by FID signals from variable-flip-angle refocusing RF pulses is shown in Figure 12. The figure shows a central coronal slice from a T2-weighted FLAIR 3D-FSE acquisition of the whole head for which a variable-flip-angle series similar to that shown in Figure 6d (left column) was used. The artifact appears as an intensity ripple in the subcutaneous fat at the top of the head (short arrows in Fig. 12).

Insight into the appearance and location of FID artifacts is provided by the diagram in Figure 13, which illustrates the correspondence between the undesired FID signal (light blue in Fig. 13a) and the desired echo signal (yellow in Fig. 13a) in relation to the refocusing RF pulses and spatial-encoding gradients of a 3D-FSE pulse sequence. The FID signal originates at the refocusing RF pulse, whereas the echo signal is centered between successive RF pulses. In Figure 13b, the two series of concentric circles (i.e., the light blue and yellow "bull's-eye" patterns) show, in concept, a plane of *k*-space data corresponding to the FID

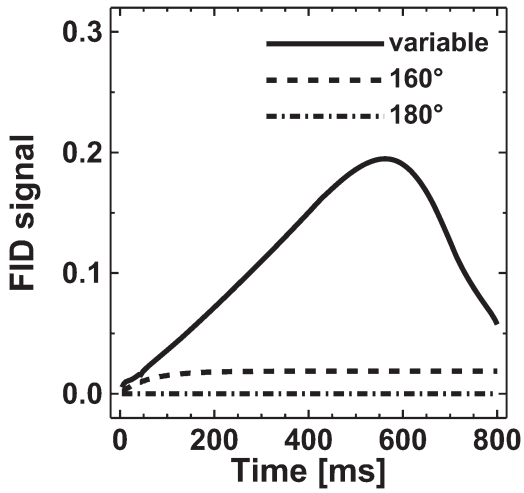

Figure 11. Free-induction-decay (FID) signals generated by refocusing RF pulses with flip-angle values less than 180°. The plot shows FID signals generated during an 800-ms echo train for constant 180° refocusing RF pulses (dot-dashed line), constant 160° refocusing RF pulses (dashed line), and flip angles that vary throughout the echo train (solid line; same flip-angle values as those shown in Fig. 6d, left column). While relatively high refocusing-RF-pulse flip angles generate minimal FID signals, low refocusing-RF-pulse flip angles may generate FID signals comparable in amplitude to the echo signals generated during the echo train. (Echo-train length, 200; echo spacing, 4 ms; T1/T2, 300/60 ms; repetition time long relative to T1.)

(light blue) and echo (yellow); the readout direction is horizontal and the in-plane phase-encoding direction is vertical in the figure. Because phase-encoding gradients are applied within each echo spacing of an FSE pulse sequence, the FID signal is spatially encoded along all three directions, just like the echo signal. (This is in contrast to a conventional spin-echo pulse sequence, wherein any FID signal from the refocusing RF pulse is not phase-encoded because the phase-encoding gradient occurs before the refocusing RF pulse, and thus the associated artifact appears as a line ["zipper"] across the image.) However, for the gradient configuration shown in Figure 13, the center of *k*-space for the FID signal is immediately after the RF pulse whereas that for the echo signal is at the center of the readout gradient. Thus, considering the region of *k*-space sampled to create the image set (denoted by the white square in Fig. 13b), only high spatial frequency data along the readout direction are captured for the FID signals. Recall that high spatial frequency data (i.e., the periphery of *k*-space) represent edge information in the image. Because, for the FIDs, the sampled data include only the high spatial frequencies, and because the FID signals are strong only for tissues that have a relatively short T1 relaxation time (i.e., fat), the sampled FID signals generate an image containing only the edges (rapid changes in signal intensity) of tissues with a short T1 value; this "edge" image from the FID signals is superimposed on the desired image. Furthermore, because not all high spatial frequency data are captured for the FID signals, but only that along the direction corresponding to the readout gradient, as noted above, the edge image contains only edges that have a component perpendicular to the readout direction. This is why, in Figure 12, the artifact is seen at the top of the head, but not at either side of the head. Finally, because the *k*-space for the FID signals is displaced in time relative to that for the echo signals, the edge artifact from fat creates an interference pattern with the signals from the echo, resulting in the intensity ripples seen in Figure 12.

For the two phase-encoding directions, the gradient waveforms shown in Figure 13 have a net area of zero over one echo spacing, whereas the net area is non-zero for the readout gradient waveform. The effect of the non-zero area for the readout gradient waveform is to displace the *k*-space for the FID signals (light blue bull's eye) along the readout direction from that for the echo signals (yellow bull's eye) as illustrated in Figure 13b, and thus for our example the FID artifact appears at edges oriented perpendicular to the readout direction, as described above. The pulse sequence could be modified to have a net gradient area along any desired axis, or along multiple axes, by including appropriate spoiler (crusher) gradients, which serve to displace the *k*-space corresponding to the FID signals away from that for the echo signals along the desired direction. In this way, one can control the edges at which FID artifacts may appear. (For example, if the pulse sequence were modified to have a balanced

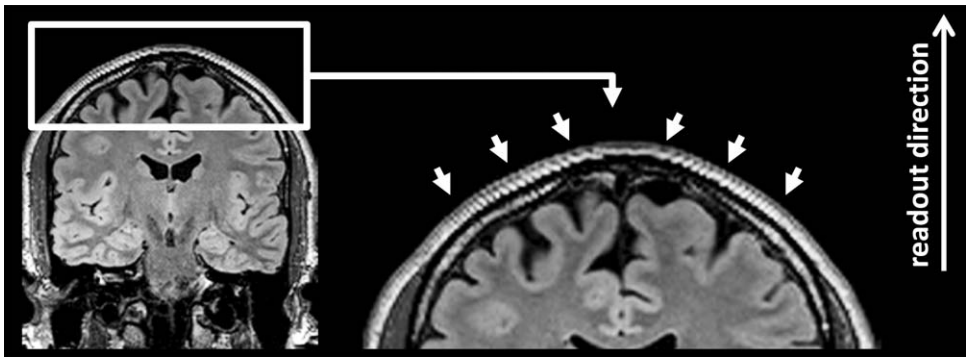

Figure 12. Artifact in single-slab 3D FSE from FID signals generated by variable-flip-angle refocusing RF pulses. A coronal T2-weighted FLAIR brain image is shown from a single-slab 3D-FSE acquisition of the whole head using variable-flip-angle refocusing RF pulses. The FID artifact appears as intensity ripples in the subcutaneous fat, indicated by the short arrows. The readout direction for the acquisition was head-to-foot.

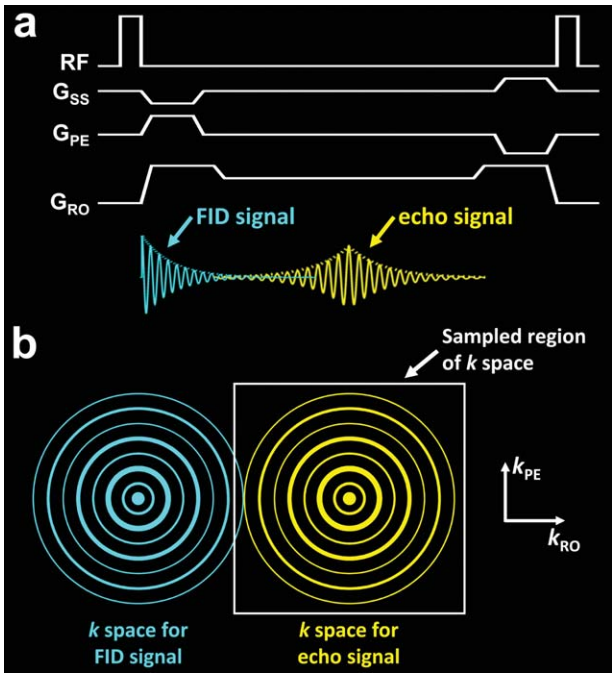

Figure 13. Relationship between FID and echo signals during a 3D-FSE echo train. **a:** The pulse-sequence diagram for one echo spacing of single-slab 3D FSE is shown to illustrate the timing of the FID (light blue) and echo (yellow) signals relative to the refocusing RF pulses and spatial-encoding gradients. **b:** The two series of concentric circles (that resemble "bull's-eye" patterns) represent a plane of *k*-space data for the FID (light blue) and echo (yellow) signals. The *k*-space data for the FID signals are displaced along the readout direction from that for the echo signals because the area under the readout gradient waveform is not zero. The series of refocusing RF pulses applied in an FSE echo train also creates echoes of the FID signals, which have a maximum value just before each refocusing RF pulse. (That is, these echoes of FID signals appear similar to the FID signals, but mirrored about the center of the readout gradient.) For simplicity, these signals are omitted from the diagram, although they also participate in the generation of FID artifacts in the image. (RF, radio frequency; G_{SS}, slice-select gradient; G_{PE}, in-plane phase-encoding gradient; G_{RO}, readout [frequency-encoding] gradient.)

[zero area] readout gradient, and to include spoiler gradients along the phase-encoding axis corresponding to the left–right direction in Figure 12, one would observe FID artifacts [intensity ripples] in the subcutaneous fat at the sides of the head instead of at the top of the head.) In addition, by increasing the net area over the echo spacing for a given gradient direction, the intensity of FID artifacts can be attenuated at the cost of slightly increasing the minimum echo spacing. Furthermore, by acquiring two averages (i.e., two NEX) and alternating the phase of the refocusing RF pulses by 180° between averages, the FID signals will cancel, thereby completely eliminating FID artifacts (115,116).

In summary, FID artifacts may appear when one or more of the T1 relaxation times corresponding to tissues in the volume of interest are relatively short and, at the same time, relatively low flip angles are used for the refocusing RF pulses. In contrast to the well-known FID artifacts for conventional spin-echo imaging, 3D-FSE FID artifacts follow the underlying anatomy and thus do not generally appear as straight lines in the image. The configuration of the gradient waveforms in the pulse sequence determines at which edges associated with short-T1 tissues artifacts may appear. FID artifacts can be attenuated by increasing the spoiler (crusher) gradients applied in the pulse sequence, or completely eliminated by data averaging. With appropriate pulse-sequence design, FID artifacts are typically negligible. Nonetheless, the radiologist should be aware of the potential for these artifacts because they have an appearance different than that for other common MRI artifacts. To determine if some structure or pattern in the image arises from FID artifacts, one can repeat the acquisition with two averages to eliminate FID contributions. (This assumes the scanner manufacturer has properly configured the pulse sequence to eliminate FID signals when two averages are used, which can be verified using a water phantom.)

Slab-Selective Imaging

Although non–spatially selective RF pulses are very useful for increasing the efficiency of single-slab 3D-FSE imaging, many clinical applications are challenging to perform effectively without some degree of spatial selectivity. Several approaches have been developed to provide spatial selection for 3D FSE while still permitting non–spatially selective refocusing RF pulses to be used. All of these methods use an excitation RF pulse that is spatially selective in one (115–118) or more (23,99,117) dimensions. "Inner-volume" approaches (119) for 3D FSE, which achieve selectively in two directions by using slab-selective excitation along one direction in conjunction with a first refocusing RF pulse that is selective along an orthogonal direction, have also been demonstrated (117,118,120).

No matter how spatial selectivity is achieved, an important requirement is to maintain the short echo spacing permitted by non–spatially selective refocusing RF pulses even though the excitation RF pulse may be relatively long. A straightforward approach for achieving this goal is illustrated in Figure 14, which shows slab-selective 3D-FSE imaging based on an excitation RF pulse that is spatially selective along one direction (115,116). A relatively long echo spacing (ESP_1 in Fig. 14) is used for the first echo (117,121) to accommodate the long slab-selective excitation RF pulse, while a shorter echo spacing (ESP_2 in Fig. 14) is used for the second and subsequent echoes, as described for 3D FSE by Mitsouras et al (117), thereby maintaining the efficiency provided by non–spatially selective refocusing RF pulses. To prevent stimulated echoes associated with the first echo spacing from appearing later in the echo train, the flip angle for the first refocusing RF pulse should be relatively high (ideally, 180°), and spoiler (crusher) gradients are applied before and after the RF pulse. (Stimulated echoes associated with the first echo spacing need to be suppressed because they would not rephase at the same time as those generated subsequently in the echo train, because the first echo spacing is longer

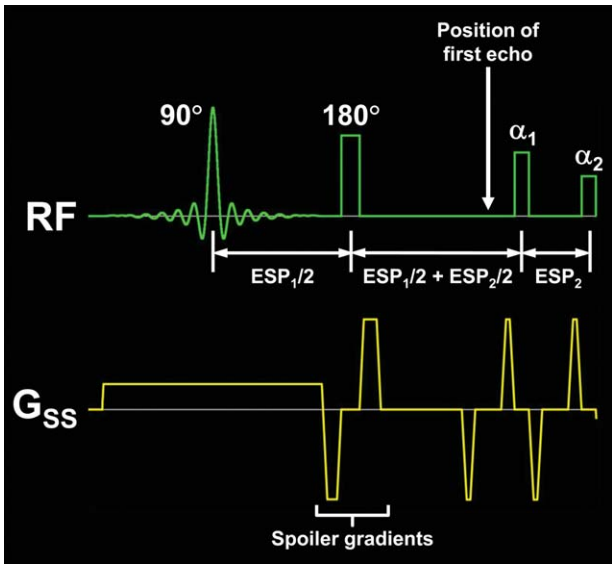

Figure 14. Efficient slab-selective 3D-FSE imaging. The pulse-sequence timing diagram is shown for one of several approaches to achieve slab-selective, single-slab 3D-FSE imaging. For this example, spatial selection along the through-plane phase-encoding direction is obtained using a slab-selective 90° excitation RF pulse. The spin echo generated by the excitation and first refocusing RF pulses occurs at the time indicated by the vertical white arrow. The first echo spacing (ESP_1) is thus much longer than the second and subsequent echo spacings (ESP_2). To prevent stimulated echoes associated with the first echo spacing from appearing later in the echo train, the flip angle for the first refocusing RF pulse is 180° (ideally, this RF pulse would not store transverse magnetization along the longitudinal axis to subsequently form a stimulated echo), and spoiler (crusher) gradients are applied before and after the RF pulse to account for nonideal deviations in the flip-angle value from 180° due to sources such as transmitter miscalibration or B1 inhomogeneity. The gradient waveform shown just before the first refocusing RF pulse combines the slice-select rephasing gradient (negative) and the spoiler gradient (positive); the net value is negative because the area required for the former is larger than that for the latter for this example. (RF, radio frequency; G_{SS}, slice-select gradient; ESP, echo spacing.)

than the other echo spacings.) Although the refocusing RF pulses are, in concept, non–spatially selective because a slice-selection gradient is not applied in conjunction with the pulses, their performance is affected by static field inhomogeneity (e.g., see Fig. 3 in Fleysher et al) (122), and the anticipated degree of field inhomogeneity should be considered when selecting the RF-pulse bandwidths. In particular, for the slab-selective implementation described here, intensity shading from static field inhomogeneity may be observed across the image volume if the bandwidth for the first refocusing RF pulse is insufficient. This can occur because field inhomogeneity causes the flip angle resulting from the RF pulse to deviate substantially from 180°, which in return reduces the fraction of magnetization refocused (Fig. 4b).

An important practical aspect of slab-selective 3D FSE involves FID artifacts. Because the non–spatially selective refocusing RF pulses affect all tissue within the sensitive volume of the RF coil used for transmission, FID artifacts can originate from edges outside of the volume of interest and alias into the images. For this situation, the artifacts would not typically appear at an edge in the image (as illustrated in Fig. 12), but instead could appear within tissue unrelated to the source of the artifact. The application of spatial presaturation RF pulses to tissue outside of the volume of interest can, in many cases, suppress these artifacts (118). However, if the T1 relaxation time corresponding to a tissue outside of the volume of interest is relatively short and, at the same time, relatively low flip angles are used for the refocusing RF pulses, artifacts may still appear because substantial longitudinal magnetization will regrow during the echo train, as described in the previous section. In this case, spatial presaturation RF pulses applied before the echo train will be ineffective; however data averaging will suppress the artifacts.

Figure 15 shows an example of FID artifacts originating from outside the slab of interest. T2-weighted, variable-flip-angle 3D-FSE images (echo train duration 745 ms) were obtained of a small plastic bottle positioned next to a short cylinder (Fig. 15a), both of which contained water doped to yield a relatively short T1. As illustrated by the white box in Figure 15a, slab-selective 3D-FSE image sets were obtained of the short cylinder, with the readout direction left-to-right for the images shown in Figure 15b. For this example, spoiler gradients within each echo spacing were applied along the readout direction, consistent with Figures 12 and 13. FID artifacts, appearing as intensity ripples in the otherwise uniform signal in an image slice through the short cylinder, are seen from the edges of the body of the bottle (Fig. 15b, arrows) and from the neck of the bottle (Fig. 15b, arrowheads). As seen in the lower right image of Figure 15b, two averages eliminates the FID artifacts. Nonetheless, because the acquisition of two averages of course doubles the imaging time, it would be desirable to eliminate the artifacts with less of a time penalty. One approach for achieving this goal is to perform "partial" averaging wherein one complete dataset plus one partial dataset is collected. (Ideally, the portion of data for which two averages are acquired includes that containing the bulk of the artifact energy. Referring to Figure 13b, one should include the phase-encoding lines corresponding to the region of *k*-space wherein the FID signals [light blue] make the greatest contribution to the sampled-data region, as marked by the white box.) For example, a 1.4 average dataset (Fig. 15b, upper right) includes one complete dataset and the central 40% (along the through-plane phase-encoding direction for this pulse sequence configuration) of a second dataset. As seen in Figure 15b, 1.4 averages substantially reduce the artifacts, and for 1.7 averages the artifacts are barely visible within the uniform background of the water phantom.

CONCLUSIONS

Spin-echo-based acquisitions remain the workhorse of clinical MRI as they provide a variety of useful

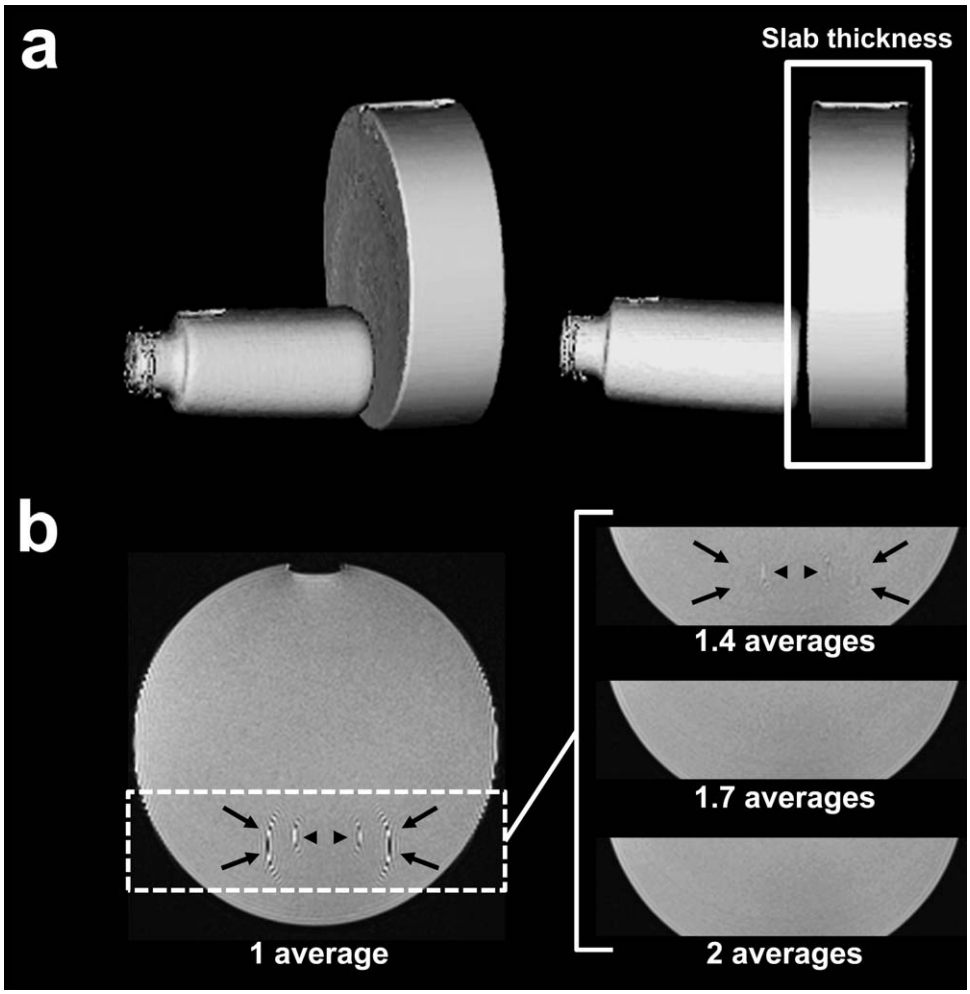

Figure 15. Partial averaging to suppress out-of-slab FID artifacts generated in slab-selective 3D FSE using variable-flip-angle refocusing RF pulses. Images of water phantoms are shown from T2-weighted, variable-flip-angle 3D-FSE acquisitions (echo train duration, 745 ms; TE_{eff} 377 ms; readout direction, left-to-right for images in part (b)). **a:** Volume-rendered images are shown to illustrate the relationship between the small plastic bottle positioned next to a short cylinder, both of which contained doped water. **b:** Slab-selective 3D-FSE imaging was performed using the slab thickness indicated by the white rectangle in (a). FID artifacts, aliased from outside of the slab, are clearly visible (arrows and arrowheads) in the image on the left, acquired with one average. The outer set of artifacts (arrows) originates from the edges of the body of the bottle and the inner set (arrowheads) originates from the edges of the neck of the bottle. The artifacts are mostly suppressed by 1.4 averages and essentially eliminated with 1.7 averages.

image contrasts and are resistant to image artifacts from RF or static field inhomogeneity. Furthermore, 3D acquisitions, which provide datasets that can be retrospectively reformatted for viewing in freely selectable orientations, are advantageous for evaluating the complex anatomy associated with many applications of MRI. Herein, we have described how fast-spin-echo pulse sequences can be designed and optimized to permit true (single-slab) 3D acquisitions with clinically practical acquisition times. These optimized techniques are compatible with other established methods for manipulating contrast, such as inversion recovery (8,108), fat suppression, or fat-water separation (123,124). For example, the 3D approach is particularly useful for performing fluid-attenuated inversion recovery (FLAIR) imaging in the brain, because the whole-brain acquisition suppresses flow-related artifacts (e.g., in the subarachnoid space and ventricles) that commonly occur in 2D-based methods (8). Overall, optimized single-slab 3D FSE provides a flexible and robust approach for 3D spin-echo-based imaging with a broad range of clinical applications.

ACKNOWLEDGMENT

The author thanks Dr. James Brookeman for helpful discussions during preparation of the manuscript.

REFERENCES

1. Hennig J, Nauerth A, Friedburg H. RARE imaging: a fast imaging method for clinical MR. Magn Reson Med 1986;3:823–833.
2. Jack CR Jr, Bernstein MA, Fox NC, et al. The Alzheimer's Disease Neuroimaging Initiative (ADNI): MRI methods. J Magn Reson Imaging 2008;27:685–691.
3. Oshio K, Jolesz FA, Melki PS, Mulkern RV. T2-weighted thin-section imaging with the multislab three-dimensional RARE technique. J Magn Reson Imaging 1991;1:695–700.
4. Yuan C, Schmiedl UP, Weinberger E, Krueck WR, Rand SD. Three-dimensional fast spin-echo imaging: pulse sequence and in vivo image evaluation. J Magn Reson Imaging 1993;3:894–899.
5. Liu K, Xu Y, Loncar M. Reduced slab boundary artifact in multi-slab 3D fast spin-echo imaging. Magn Reson Med 2000;44:269–276.
6. Kholmovski EG, Alexander AL, Parker DL. Correction of slab boundary artifact using histogram matching. J Magn Reson Imaging 2002;15:610–617.
7. Mugler JP III, Bao S, Mulkern RV, et al. Optimized single-slab three-dimensional spin-echo MR imaging of the brain. Radiology 2000;216:891–899.
8. Kallmes DF, Hui FK, Mugler JP III. Suppression of cerebrospinal fluid and blood flow artifacts in FLAIR MR imaging with a single-slab three-dimensional pulse sequence: initial experience. Radiology 2001;221:251–255.
9. Bink A, Schmitt M, Gaa J, Mugler JP III, Lanfermann H, Zanella FE. Detection of lesions in multiple sclerosis by 2D FLAIR and single-slab 3D FLAIR sequences at 3.0 T: initial results. Eur Radiol 2006;16:1104–1110.
10. Pouwels PJ, Kuijer JP, Mugler JP III, Guttmann CR, Barkhof F. Human gray matter: feasibility of single-slab 3D double inversion-recovery high-spatial-resolution MR imaging. Radiology 2006;241:873–879.

11. Chagla GH, Busse RF, Sydnor R, Rowley HA, Turski PA. Three-dimensional fluid attenuated inversion recovery imaging with isotropic resolution and nonselective adiabatic inversion provides improved three-dimensional visualization and cerebrospinal fluid suppression compared to two-dimensional FLAIR at 3 Tesla. Invest Radiol 2008;43:547–551.
12. Komada T, Naganawa S, Ogawa H, et al. Contrast-enhanced MR imaging of metastatic brain tumor at 3 tesla: utility of T1-weighted SPACE compared with 2D spin echo and 3D gradient echo sequence. Magn Reson Med Sci 2008;7:13–21.
13. Moraal B, Wattjes MP, Geurts JJ, et al. Improved detection of active multiple sclerosis lesions: 3D subtraction imaging. Radiology 2010;255:154–163.
14. Naganawa S, Ishihara S, Iwano S, Sone M, Nakashima T. Three-dimensional (3D) visualization of endolymphatic hydrops after intratympanic injection of Gd-DTPA: optimization of a 3D-real inversion-recovery turbo spin-echo (TSE) sequence and application of a 32-channel head coil at 3T. J Magn Reson Imaging 2010;31:210–214.
15. Naganawa S, Kawai H, Sone M, Nakashima T. Increased sensitivity to low concentration gadolinium contrast by optimized heavily T2-weighted 3D-FLAIR to visualize endolymphatic space. Magn Reson Med Sci 2010;9:73–80.
16. Park J, Kim EY. Contrast-enhanced, three-dimensional, whole-brain, black-blood imaging: application to small brain metastases. Magn Reson Med 2010;63:553–561.
17. Roosendaal SD, Hulst HE, Vrenken H, et al. Structural and functional hippocampal changes in multiple sclerosis patients with intact memory function. Radiology 2010;255:595–604.
18. Visser F, Zwanenburg JJ, Hoogduin JM, Luijten PR. High-resolution magnetization-prepared 3D-FLAIR imaging at 7.0 Tesla. Magn Reson Med 2010;64:194–202.
19. Aiken AH, Mukherjee P, Green AJ, Glastonbury CM. MR imaging of optic neuropathy with extended echo-train acquisition fluid-attenuated inversion recovery. AJNR Am J Neuroradiol 2011;32: 301–305.
20. Cha J, Kim ST, Kim HJ, et al. Trigeminal neuralgia: assessment with T2 VISTA and FLAIR VISTA fusion imaging. Eur Radiol 2011;21:2633–2639.
21. Lummel N, Schoepf V, Burke M, Brueckmann H, Linn J. 3D fluid-attenuated inversion recovery imaging: reduced CSF artifacts and enhanced sensitivity and specificity for subarachnoid hemorrhage. AJNR Am J Neuroradiol 2011;32:2054–2060.
22. Nam Y, Kim EY, Kim DH. On the use of a spin-echo based double inversion recovery acquisition for the measurement of cortical brain thickness. J Magn Reson Imaging 2011;33:1218–1223.
23. Sarkar SN, Alsop DC, Madhuranthakam AJ, et al. Brain MR imaging at ultra-low radiofrequency power. Radiology 2011;259: 550–557.
24. de Graaf WL, Zwanenburg JJ, Visser F, et al. Lesion detection at seven Tesla in multiple sclerosis using magnetisation prepared 3D-FLAIR and 3D-DIR. Eur Radiol 2012;22:221–231.
25. Kitajima M, Hirai T, Shigematsu Y, et al. Comparison of 3D FLAIR, 2D FLAIR, and 2D T2-weighted MR imaging of brain stem anatomy. AJNR Am J Neuroradiol 2012;33:922–927.
26. Zwanenburg JJ, Hendrikse J, Luijten PR. Generalized multiple-layer appearance of the cerebral cortex with 3D FLAIR 7.0-T MR imaging. Radiology 2012;262:995–1001.
27. Kilsdonk ID, de Graaf WL, Soriano AL, et al. Multicontrast MR imaging at 7T in multiple sclerosis: highest lesion detection in cortical gray matter with 3D-FLAIR. AJNR Am J Neuroradiol 2013;34:791–796.
28. Yoshida A, Tha KK, Fujima N, et al. Detection of brain metastases by 3-dimensional magnetic resonance imaging at 3 T: comparison between T1-weighted volume isotropic turbo spin echo acquisition and 3-dimensional T1-weighted fluid-attenuated inversion recovery imaging. J Comput Assist Tomogr 2013;37:84–90.
29. Baumert B, Wortler K, Steffinger D, Schmidt GP, Reiser MF, Baur-Melnyk A. Assessment of the internal craniocervical ligaments with a new magnetic resonance imaging sequence: three-dimensional turbo spin echo with variable flip-angle distribution (SPACE). Magn Reson Imaging 2009;27:954–960.
30. Kwon JW, Yoon YC, Choi SH. Three-dimensional isotropic T2-weighted cervical MRI at 3T: comparison with two-dimensional T2-weighted sequences. Clin Radiol 2012;67:106–113.
31. Lichy MP, Wietek BM, Mugler JP III, et al. Magnetic resonance imaging of the body trunk using a single-slab, 3-dimensional, T2-weighted turbo-spin-echo sequence with high sampling efficiency (SPACE) for high spatial resolution imaging: initial clinical experiences. Invest Radiol 2005;40:754–760.
32. Viallon M, Vargas MI, Jlassi H, Lovblad KO, Delavelle J. High-resolution and functional magnetic resonance imaging of the brachial plexus using an isotropic 3D T2 STIR (Short Term Inversion Recovery) SPACE sequence and diffusion tensor imaging. Eur Radiol 2008;18:1018–1023.
33. Agrawal G, Riherd JM, Busse RF, Hinshaw JL, Sadowski EA. Evaluation of uterine anomalies: 3D FRFSE CUBE versus standard 2D FRFSE. AJR Am J Roentgenol 2009;193:W558–W562.
34. Morita S, Ueno E, Masukawa A, et al. Comparison of SPACE and 3D TSE MRCP at 1.5T focusing on difference in echo spacing. Magn Reson Med Sci 2009;8:101–105.
35. Arizono S, Isoda H, Maetani YS, et al. High spatial resolution 3D MR cholangiography with high sampling efficiency technique (SPACE): comparison of 3T vs. 1.5T. Eur J Radiol 2010;73:114–118.
36. Kim H, Lim JS, Choi JY, et al. Rectal cancer: comparison of accuracy of local-regional staging with two- and three-dimensional preoperative 3-T MR imaging. Radiology 2010;254:485–492.
37. Rosenkrantz AB, Neil J, Kong X, et al. Prostate cancer: comparison of 3D T2-weighted with conventional 2D T2-weighted imaging for image quality and tumor detection. AJR Am J Roentgenol 2010;194:446–452.
38. Rosenkrantz AB, Patel JM, Babb JS, Storey P, Hecht EM. Liver MRI at 3 T using a respiratory-triggered time-efficient 3D T2-weighted technique: impact on artifacts and image quality. AJR Am J Roentgenol 2010;194:634–641.
39. Hecht EM, Yitta S, Lim RP, et al. Preliminary clinical experience at 3 T with a 3D T2-weighted sequence compared with multiplanar 2D for evaluation of the female pelvis. AJR Am J Roentgenol 2011;197:W346–W352.
40. Hori M, Kim T, Onishi H, et al. Uterine tumors: comparison of 3D versus 2D T2-weighted turbo spin-echo MR imaging at 3.0 T–initial experience. Radiology 2011;258:154–163.
41. Manganaro L, Fierro F, Tomei A, et al. Feasibility of 3.0T pelvic MR imaging in the evaluation of endometriosis. Eur J Radiol 2012;81:1381–1387.
42. Tagliafico A, Succio G, Neumaier CE, et al. Brachial plexus assessment with three-dimensional isotropic resolution fast spin echo MRI: comparison with conventional MRI at 3.0 T. Br J Radiol 2012;85:e110–e116.
43. Kijowski R, Gold GE. Routine 3D magnetic resonance imaging of joints. J Magn Reson Imaging 2011;33:758–771.
44. Gold GE, Busse RF, Beehler C, et al. Isotropic MRI of the knee with 3D fast spin-echo extended echo-train acquisition (XETA): initial experience. AJR Am J Roentgenol 2007;188:1287–1293.
45. Jung JY, Yoon YC, Kwon JW, Ahn JH, Choe BK. Diagnosis of internal derangement of the knee at 3.0-T MR imaging: 3D isotropic intermediate-weighted versus 2D sequences. Radiology 2009;253:780–787.
46. Kijowski R, Davis KW, Woods MA, et al. Knee joint: comprehensive assessment with 3D isotropic resolution fast spin-echo MR imaging--diagnostic performance compared with that of conventional MR imaging at 3.0 T. Radiology 2009;252:486–495.
47. Notohamiprodjo M, Horng A, Pietschmann MF, et al. MRI of the knee at 3T: first clinical results with an isotropic PDfs-weighted 3D-TSE-sequence. Invest Radiol 2009;44:585–597.
48. Chen CA, Kijowski R, Shapiro LM, et al. Cartilage morphology at 3.0T: assessment of three-dimensional magnetic resonance imaging techniques. J Magn Reson Imaging 2010;32:173–183.
49. Seo JM, Yoon YC, Kwon JW. 3D isotropic turbo spin-echo intermediate-weighted sequence with refocusing control in knee imaging: comparison study with 3D isotropic fast-field echo sequence. Acta Radiol 2011;52:1119–1124.
50. Welsch GH, Zak L, Mamisch TC, et al. Advanced morphological 3D magnetic resonance observation of cartilage repair tissue (MOCART) scoring using a new isotropic 3D proton-density, turbo spin echo sequence with variable flip angle distribution (PD-SPACE) compared to an isotropic 3D steady-state free precession sequence (True-FISP) and standard 2D sequences. J Magn Reson Imaging 2011;33:180–188.
51. Ai T, Zhang W, Priddy NK, Li X. Diagnostic performance of CUBE MRI sequences of the knee compared with conventional MRI. Clin Radiol 2012;67:e58–e63.

52. Jung JY, Jee WH, Park MY, Lee SY, Kim JM. Meniscal tear configurations: categorization with 3D isotropic turbo spin-echo MRI compared with conventional MRI at 3 T. AJR Am J Roentgenol 2012;198:W173–W180.
53. Kijowski R, Davis KW, Blankenbaker DG, Woods MA, Del Rio AM, De Smet AA. Evaluation of the menisci of the knee joint using three-dimensional isotropic resolution fast spin-echo imaging: diagnostic performance in 250 patients with surgical correlation. Skeletal Radiol 2012;41:169–178.
54. Lefevre N, Naouri JF, Bohu Y, Klouche S, Herman S. Partial tears of the anterior cruciate ligament: diagnostic performance of isotropic three-dimensional fast spin echo (3D-FSE-CUBE) MRI. Eur J Orthop Surg Traumatol 2012. doi:10.1007/s00590-00012-01135-00594
55. Notohamiprodjo M, Horng A, Kuschel B, et al. 3D-imaging of the knee with an optimized 3D-FSE-sequence and a 15-channel knee-coil. Eur J Radiol 2012;81:3441–3449.
56. Stevens KJ, Busse RF, Han E, et al. Ankle: isotropic MR imaging with 3D-FSE-CUBE--initial experience in healthy volunteers. Radiology 2008;249:1026–1033.
57. Kim HS, Yoon YC, Kwon JW, Choe BK. Qualitative and quantitative assessment of isotropic ankle magnetic resonance imaging: three-dimensional isotropic intermediate-weighted turbo spin echo versus three-dimensional isotropic fast field echo sequences. Korean J Radiol 2012;13:443–449.
58. Notohamiprodjo M, Kuschel B, Horng A, et al. 3D-MRI of the ankle with optimized 3D-SPACE. Invest Radiol 2012;47:231–239.
59. Choo HJ, Lee SJ, Kim OH, Seo SS, Kim JH. Comparison of three-dimensional isotropic T1-weighted fast spin-echo MR arthrography with two-dimensional MR arthrography of the shoulder. Radiology 2012;262:921–931.
60. Jung JY, Jee WH, Park MY, Lee SY, Kim YS. Supraspinatus tendon tears at 3.0 T shoulder MR arthrography: diagnosis with 3D isotropic turbo spin-echo SPACE sequence versus 2D conventional sequences. Skeletal Radiol 2012;41:1401–1410.
61. Jung JY, Jee WH, Park MY, Lee SY, Kim YS. SLAP tears: diagnosis using 3-T shoulder MR arthrography with the 3D isotropic turbo spin-echo space sequence versus conventional 2D sequences. Eur Radiol 2013;23:487–495.
62. Stevens KJ, Wallace CG, Chen W, Rosenberg JK, Gold GE. Imaging of the wrist at 1.5 Tesla using isotropic three-dimensional fast spin echo cube. J Magn Reson Imaging 2011;33:908–915.
63. Jung JY, Yoon YC, Jung JY, Choe BK. Qualitative and quantitative assessment of wrist MRI at 3.0T: comparison between isotropic 3D turbo spin echo and isotropic 3D fast field echo and 2D turbo spin echo. Acta Radiol 2013;54:284–291.
64. Lim RP, Storey P, Atanasova IP, et al. Three-dimensional electrocardiographically gated variable flip angle FSE imaging for MR angiography of the hands at 3.0 T: initial experience. Radiology 2009;252:874–881.
65. Mihai G, Chung YC, Kariisa M, Raman SV, Simonetti OP, Rajagopalan S. Initial feasibility of a multi-station high resolution three-dimensional dark blood angiography protocol for the assessment of peripheral arterial disease. J Magn Reson Imaging 2009;30:785–793.
66. Lanzman RS, Blondin D, Schmitt P, et al. Non-enhanced 3D MR angiography of the lower extremity using ECG-gated TSE imaging with non-selective refocusing pulses--initial experience. RoFo 2010;182:861–867.
67. Mihai G, Chung YC, Merchant A, Simonetti OP, Rajagopalan S. T1-weighted-SPACE dark blood whole body magnetic resonance angiography (DB-WBMRA): initial experience. J Magn Reson Imaging 2010;31:502–509.
68. Morita S, Kojima S, Hirata M, et al. Unenhanced ECG-gated fast spin-echo MR digital subtraction angiography (MRDSA) using short echo-spacing three-dimensional sequence of femoral arteries: initial experience. J Magn Reson Imaging 2011;34:157–164.
69. Mihai G, Winner MW, Raman SV, Rajagopalan S, Simonetti OP, Chung YC. Assessment of carotid stenosis using three-dimensional T2-weighted dark blood imaging: initial experience. J Magn Reson Imaging 2012;35:449–455.
70. Diop AD, Braidy C, Habouchi A, et al. Unenhanced 3D turbo spin-echo MR angiography of lower limbs in peripheral arterial disease: a comparative study with gadolinium-enhanced MR angiography. AJR Am J Roentgenol 2013;200:1145–1150.
71. Lim RP, Fan Z, Chatterji M, et al. Comparison of nonenhanced MR angiographic subtraction techniques for infragenual arteries at 1.5 T: a preliminary study. Radiology 2013;267:293–304.
72. Sakurai K, Miura T, Sagisaka T, et al. Evaluation of luminal and vessel wall abnormalities in subacute and other stages of intracranial vertebrobasilar artery dissections using the volume isotropic turbo-spin-echo acquisition (VISTA) sequence: a preliminary study. J Neuroradiol 2013;40:19–28.
73. Zhang Z, Fan Z, Carroll TJ, et al. Three-dimensional T2-weighted MRI of the human femoral arterial vessel wall at 3.0 Tesla. Invest Radiol 2009;44:619–626.
74. Fan Z, Zhang Z, Chung YC, et al. Carotid arterial wall MRI at 3T using 3D variable-flip-angle turbo spin-echo (TSE) with flow-sensitive dephasing (FSD). J Magn Reson Imaging 2010;31:645–654.
75. Parmar JP, Rogers WJ, Mugler JP III, et al. Magnetic resonance imaging of carotid atherosclerotic plaque in clinically suspected acute transient ischemic attack and acute ischemic stroke. Circulation 2010;122:2031–2038.
76. Qiao Y, Steinman DA, Qin Q, et al. Intracranial arterial wall imaging using three-dimensional high isotropic resolution black blood MRI at 3.0 Tesla. J Magn Reson Imaging 2011;34:22–30.
77. Mulkern RV, Wong ST, Winalski C, Jolesz FA. Contrast manipulation and artifact assessment of 2D and 3D RARE sequences. Magn Reson Imaging 1990;8:557–566.
78. Melki PS, Jolesz FA, Mulkern RV. Partial RF echo planar imaging with the FAISE method. I. Experimental and theoretical assessment of artifact. Magn Reson Med 1992;26:328–341.
79. Constable RT, Anderson AW, Zhong J, Gore JC. Factors influencing contrast in fast spin-echo MR imaging. Magn Reson Imaging 1992;10:497–511.
80. Jones KM, Mulkern RV, Schwartz RB, Oshio K, Barnes PD, Jolesz FA. Fast spin-echo MR imaging of the brain and spine: current concepts. AJR Am J Roentgenol 1992;158:1313–1320.
81. Jones KM, Mulkern RV, Mantello MT, et al. Brain hemorrhage: evaluation with fast spin-echo and conventional dual spin-echo images. Radiology 1992;182:53–58.
82. Melki PS, Jolesz FA, Mulkern RV. Partial RF echo-planar imaging with the FAISE method. II. Contrast equivalence with spin-echo sequences. Magn Reson Med 1992;26:342–354.
83. Melki PS, Mulkern RV. Magnetization transfer effects in multi-slice RARE sequences. Magn Reson Med 1992;24:189–195.
84. Hahn EL. Spin echoes. Phys Rev 1950;80:580–594.
85. Woessner DE. Effects of diffusion in nuclear magnetic resonance spin-echo experiments. J Chem Phys 1961;34:2057–2061.
86. Hennig J. Echoes—how to generate, recognize, use or avoid them in MR-imaging sequences. Part II. Echoes in imaging sequences. Concepts Magn Reson 1991;3:179–192.
87. Wielopolski P, Achten E, de Groot JC, et al. A dual echo three-dimensional inversion recovery HASTE sequence: initial experience and potential applications for the quantification of white matter lesions and brain tissue volumes. In: Proceedings of the 4th Annual Meeting of ISMRM, New York, New York, 1996. (abstract 554).
88. Mugler JP III, Brookeman JR, Mulkern RV, Guttmann CRG, Jolesz FA. Single-slab three-dimensional spin-echo-based pulse sequences for high-resolution T1-weighted and T2-weighted imaging of the brain. In: Proceedings of the 5th Annual Meeting of ISMRM, Vancouver, BC, Canada, 1997. (abstract 137).
89. Schäffter T, Börnert P, Leibfritz D. PSF improvements in single shot GRASE imaging. In: Proceedings of the 2nd Annual Meeting of SMR, San Francisco, 1994. (abstract 27).
90. Mugler JP III, Bao S, Mulkern RV, Guttmann CRG, Jolesz FA, Brookeman JR. Three-dimensional spin-echo-train proton-density-weighted imaging using shaped signal evolutions. In: Proceedings of the 7th Annual Meeting of ISMRM, Philadelphia, 1999. (abstract 1631).
91. Mugler JP III, Kiefer B, Brookeman JR. Three-dimensional T2-weighted imaging of the brain using very long spin-echo trains. In: Proceedings of the 8th Annual Meeting of ISMRM, Denver, 2000. (abstract 687).
92. Busse RF, Hariharan H, Vu A, Brittain JH. Fast spin echo sequences with very long echo trains: design of variable refocusing flip angle schedules and generation of clinical T2 contrast. Magn Reson Med 2006;55:1030–1037.
93. Busse RF, Brau AC, Vu A, et al. Effects of refocusing flip angle modulation and view ordering in 3D fast spin echo. Magn Reson Med 2008;60:640–649.

94. Li G, Nittka M, Hollenbach H-P, et al. The shifted radial reordering for intermediate TE imaging in 3D long echo train acquisition. In: Proceedings of the 17th Annual Meeting of ISMRM, Honolulu, 2009. (abstract 2623).
95. Margosian P, Schmitt F, Purdy D. Faster MR imaging: imaging with half the data. Health Care Instrum 1986;1:195–197.
96. Feinberg DA, Hale JD, Watts JC, Kaufman L, Mark A. Halving MR imaging time by conjugation: demonstration at 3.5 kG. Radiology 1986;161:527–531.
97. Sodickson DK, Manning WJ. Simultaneous acquisition of spatial harmonics (SMASH): fast imaging with radiofrequency coil arrays. Magn Reson Med 1997;38:591–603.
98. Pruessmann KP, Weiger M, Scheidegger MB, Boesiger P. SENSE: sensitivity encoding for fast MRI. Magn Reson Med 1999;42:952–962.
99. Luk-Pat GT, Gold GE, Olcott EW, Hu BS, Nishimura DG. High-resolution three-dimensional in vivo imaging of atherosclerotic plaque. Magn Reson Med 1999;42:762–771.
100. Constable RT, Gore JC. The loss of small objects in variable TE imaging: implications for FSE, RARE, and EPI. Magn Reson Med 1992;28:9–24.
101. Ortendahl DA, Kaufman L, Kramer DM. Analysis of hybrid imaging techniques. Magn Reson Med 1992;26:155–173.
102. Hennig J. Multiecho imaging sequences with low refocusing flip angles. J Magn Reson 1988;78:397–407.
103. Alsop DC. The sensitivity of low flip angle RARE imaging. Magn Reson Med 1997;37:176–184.
104. Hennig J, Weigel M, Scheffler K. Calculation of flip angles for echo trains with predefined amplitudes with the extended phase graph (EPG)-algorithm: principles and applications to hyperecho and TRAPS sequences. Magn Reson Med 2004;51:68–80.
105. Lebel RM, Wilman AH. Intuitive design guidelines for fast spin echo imaging with variable flip angle echo trains. Magn Reson Med 2007;57:972–975.
106. Lukzen NN, Savelov AA. Analytical derivation of multiple spin echo amplitudes with arbitrary refocusing angle. J Magn Reson 2007;185:71–76.
107. Park J, Mugler JP III, Horger W, Kiefer B. Optimized T1-weighted contrast for single-slab 3D turbo spin-echo imaging with long echo trains: application to whole-brain imaging. Magn Reson Med 2007;58:982–992.
108. Park J, Park S, Kim EY, Suh JS. Phase-sensitive, dual-acquisition, single-slab, 3D, turbo-spin-echo pulse sequence for simultaneous T2-weighted and fluid-attenuated whole-brain imaging. Magn Reson Med 2010;63:1422–1430.
109. Hennig J, Scheffler K. Hyperechoes. Magn Reson Med 2001;46:6–12.
110. Hennig J, Weigel M, Scheffler K. Multiecho sequences with variable refocusing flip angles: optimization of signal behavior using smooth transitions between pseudo steady states (TRAPS). Magn Reson Med 2003;49:527–535.
111. Weigel M, Hennig J. Contrast behavior and relaxation effects of conventional and hyperecho-turbo spin echo sequences at 1.5 and 3 T. Magn Reson Med 2006;55:826–835.
112. Moseley ME, Liu C, Rodriguez S, Brosnan T. Advances in magnetic resonance neuroimaging. Neurol Clin 2009;27:1–19.
113. Mugler JP III, Menzel MI, Horger W, Kiefer B. Efficient phase-encoding for 3D turbo-spin-echo imaging with very long echo trains. In: Proceedings of the 14th Annual Meeting of ISMRM, Seattle, 2006. (abstract 2429).
114. Mugler JP III, Wald LL, Brookeman JR. T2-weighted 3D spin-echo train imaging of the brain at 3 Tesla: reduced power deposition using low flip-angle refocusing RF pulses. In: Proceedings of the 9th Annual Meeting of ISMRM, Glasgow, Scotland, 2001. (abstract 438).
115. Mugler JP III, Brookeman JR. Efficient spatially-selective single-slab 3D turbo-spin-echo imaging. In: Proceedings of the 12th Annual Meeting of ISMRM, Kyoto, Japan, 2004. (abstract 695).
116. Magland JF, Rajapakse CS, Wright AC, Acciavatti R, Wehrli FW. 3D fast spin echo with out-of-slab cancellation: a technique for high-resolution structural imaging of trabecular bone at 7 Tesla. Magn Reson Med 2010;63:719–727.
117. Mitsouras D, Mulkern RV, Rybicki FJ. Strategies for inner volume 3D fast spin echo magnetic resonance imaging using non-selective refocusing radio frequency pulses. Med Phys 2006;33:173–186.
118. Saranathan M, Hwang K, Busse R, Weishaar P, Kawashima A, Lee C. High spatial resolution, volume selective 3D FSE imaging. In: Proceedings of the 16th Annual Meeting of ISMRM, Toronto, ON, Canada, 2008. (abstract 836).
119. Feinberg DA, Hoenninger JC, Crooks LE, Kaufman L, Watts JC, Arakawa M. Inner volume MR imaging: technical concepts and their application. Radiology 1985;156:743–747.
120. Mugler JP III, Requardt M, Engelhard K, Altes TA, Paul D, Kiefer B. Inner-volume 3D turbo-spin-echo (SPACE) imaging of the prostate: preliminary experience. In: Proceedings of the 20th Annual Meeting of ISMRM, Melbourne, Australia, 2012. (abstract 3017).
121. Kanazawa H, Takai H, Machida Y, Hanawa M. Contrast naturalization of fast spin echo imaging: a fat reduction technique free from field inhomogeneity. In: Proceedings of the 2nd Annual Meeting of SMR. San Francisco, 1994. (abstract 474).
122. Fleysher R, Fleysher L, Inglese M, Sodickson D. TROMBONE: T1-relaxation-oblivious mapping of transmit radio-frequency field (B1) for MRI at high magnetic fields. Magn Reson Med 2011;66:483–491.
123. Madhuranthakam AJ, Yu H, Shimakawa A, et al. T2-weighted 3D fast spin echo imaging with water-fat separation in a single acquisition. J Magn Reson Imaging 2010;32:745–751.
124. Vasanawala SS, Madhuranthakam AJ, Venkatesan R, Sonik A, Lai P, Brau AC. Volumetric fat-water separated T2-weighted MRI. Pediatr Radiol 2011;41:875–883.
125. Mugler JP, 3rd. Motion-artifact-free T2-weighted 3D imaging of the cervical spine. In: Proceedings of the 8th Annual Meeting of ISMRM, Denver, 2000. (abstract 402).